Developing the Vibro-drill;

A feasibility study into an improved installation method for offshore foundation piles

By

B.J.M. Arntz BSc.

in partial fulfilment of the requirements for the degree of

Master of Science
in Offshore and Dredging Engineering

at the Delft University of Technology,
to be defended publicly on Thursday the 25th of January, 2018 at 15:30 AM.

Thesis committee:	Prof. Dr. A.V. Metrikine,	TU Delft
	Ass. Prof. J.S. Hoving MSc,	TU Delft
	Ass. Prof. Dr. F. Pisano	TU Delft

Abstract

To meet the demand for renewable energy sources, large numbers of offshore windfarms are planned to be constructed in the near future. The majority of the foundations for these offshore wind turbines are large-diameter monopiles. The driving of monopiles into the seabed is conventionally done using a hydraulic hammer, this process is commonly known as piling. Piling causes high noise levels that are damaging to marine life, for example it is known to cause permanent hearing loss to marine mammals. Also smaller fish are known to be affected by this noise. Piling additionally causes fatigue damage to the pile during the installation process requiring over dimensioned monopile foundations.

A potential solution to these problems is currently being developed by GBM Works; To install a monopile foundation, a set of vibrating elements is installed at the bottom of the monopile that reduce the resistance of the soil at the tip of the pile. Water is injected upwards on both sides of the pile wall to lubricate the pile-soil interface. In this way, the resistance of the soil is temporarily reduced to such an extent that the monopile foundation penetrates the soil to target depth under its own weight, thereby greatly reducing noise levels and fatigue damage.

To determine the feasibility of this installation method, an experimental study has been performed, where a prototype of one oscillating element was constructed and attached to a steel pile. Tests with this prototype were performed at the Maasvlakte, where very dense sand is found with cone resistance values of up to 30 MPa in the test depth range. Multiple experiments were conducted in which the amplitude and frequency of the vibrations were varied. Tests were done for a large range of variables in attempt to optimize the penetration speed. Additionally, based on the test results, a semi-empirical model was built to predict the installation speed of the prototype pile and to identify the influence of the different variables.

The experiments show that it is possible to penetrate the prototype pile to its full penetration of 4.5 meters into the soil. Depending on the properties of the applied oscillations and soil conditions, the penetration rates are found between 1 and 5 cm/s.

To determine the feasibility of reaching penetration depths that are similar to those of offshore foundation piles, i.e. 30 to 40 meters with larger diameter monopiles, additional experiments are required .The noise levels during the experiments were significantly lower than the noise levels for conventional piling. However, as sound in air propagates differently than in an underwater environment underwater measurements are required to further assess the noise levels of this new installation method for monopile foundations.

B.J.M. Arntz Author
Delft, January 2018

TU Delft

Acknowledgements

This research is part of a much larger undertaking that started more than two years ago. I would like to thank the people and organisations who have supported me mentally, practically and financially. Without whom this research would not have been possible in the manner it has been conducted. First of all I would like to thank Jeroen Hoving which has been not only my daily supervisor but has also helped raising the funds to construct the prototype for the experiments. The meetings and discussions were always very useful to keep me on track. And I hope that my occasional stubbornness and own way of working hasn't been too frustrating. My special appreciations go to my graduation committee Jeroen, Andrei and Federico who's thoughts and opinions were of great help to me.

I would also like to thank Nick Noordam my business partner and friend with whom I founded the company GBM Works to further develop the Vibro-drill and bring it to the market. We have had a very exciting and bumpy ride so far. It was an especially intense time during the experiment phase in august 2017 at the Maasvlakte were it was only the two of use and the prototype for an entire month of testing. Most of all I would like to thank Nick for his understanding and patience when I was working on this research, especially in the last few months which weren't easy. I would like to thank Govert Meijer for his advice, support and checking this report multiple times.

Further I would like to thank Delft Enterprises, Martine Nieuwenhuizen and Justin Kok, for their advice in financing and intellectual property. This research is also a part of the research programme Take-off phase 1 with project number 15642, which is partly financed by the Netherlands Organisation for Scientific Research (NWO).

The support I got from my girlfriend was of great importance to me. Even when working long hours she helped with her support and trust in me. Last but not least I would like to thank my parents for their faith in me during the long years I have been a student. Their support has been a pillar on which I could always rely. Further, I would like to thank my father for his efforts and advice on the design and construction of the prototype. I would like to thank my brother for the advance and guidance with this research and the company.

Contents

List of Figures

List of Tables

Abbreviations

CPT	Cone Penetration Test
dB	Decibel
Hz	Hertz
k	Kilo
kg	kilogram
KV	Kelvin-Voigt
kWh	Kilowatt hour
m	Meter
M	Million
mm	Millimeter
MPa	Mega Pascal
mT	Metric Ton
OD	Outer Diameter
OWF	Offshore Wind Farm
SEL	Sound Exposure Level
WT	Wall Thickness

List of Symbols

Symbol	Description	Unit
α	Semi-apex angle of prototype tip	deg
β	Angle resultant force and vertical	deg
γ	Strain	$[-]$
γ	Damping ratio	$[-]$
ϵ	Compression	$[-]$
θ	Angle soil reaction force to tip	deg
μ	viscosity	$Pa \cdot s$
v	Terminal velocity of particle	m/s
ρ_i	Density	kg/m^3
σ'	Effective stress in soil	kPa
σ_{total}	Total stress in soil	kPa
τ_n	Stress	kPa
φ	Angle of internal friction	rad
ω	Rotational speed	rad/s
A	Frontal surface area of the tip of the prototype	m^2
C_1	Factor for cyclic loading conditions	$[-]$
C_2	Compression constant of soil	$[-]$
B	Width of the base of the tip	m
c	Cohesion in soil	kPa
c_i	Damping constant	Ns/m
D	Depth	m
d	Diameter of particle	m
dz	Penetration of tip per cycle	m
F_{cr}	Critical yield force of soil	N
$F_{fr,applied}$	Applied force to slider-damper element	N
F_i	Force	N
f_s	Shaft friction	kPa
G_s	Secant shear modulus	N/m^2
g	Gravitational constant	m/s^2
k_i	Spring constant	N/m
L	Length of pile	m
m	Mass of tip	kg
m^*	Modal mass of pile	kg
me	Eccentric moment	$kg \cdot m$
q_c	Cone resistance	kPa
V	Shear wave velocity	m/s
x'_f	Distance of plastic deformation	m
x'_m	Distance of elastic deformation	m

1. Introduction

Offshore pile driving of large monopile foundations by hammering results in impulses that within a certain distance from the source may cause permanent hearing loss to marine mammals [1]. In order to minimize these effects on wildlife, several noise mitigation systems exist and have the potential to reduce noise emissions during impact pile driving[2]. In turn, these measures increase the installation cost of a monopile[3]. The aim of this research is to determine the feasibility of a new, potentially silent installation method for offshore foundation piles.

The problem description is given below. The proposed solution to the problem is presented in section 1.2. The aims of the thesis are further elaborated upon in section 1.3. The approach to the research is described in section 1.4. The outline of the rapport is described in section 1.5.

1.1. Problem description

Large numbers of offshore windfarms are planned to be constructed in the future to meet the demand for renewable energy sources[4]. Contractors such as Van Oord, Boskalis, Geosea and Jan de Nul install the foundation piles. They desire an installation method that is fast, simple and reliable.

The current method to install these foundation piles is by piling using a hydraulic hammer. However this method has its downsides. Challenges of the hydraulic hammer are:

1. High underwater noise levels, which is harmful for marine mammals and fish. Mitigating measures increase the operational costs.
2. Low penetration speed
3. Long handling times
4. Fatigue damage in the pile during installation causes more complex and expensive foundation piles.
5. The market demand for larger wind turbines results in larger foundation piles. When no measures are taken the upscaling of foundation piles and hydraulic hammers will soon reach its limit.

1.1.1. High underwater noise levels

High underwater noise levels can cause damage to marine mammals and fish. A number of countries in Europe have therefore stated regulations for underwater noise arising from offshore piling activities. Regulations vary per country, the countries with the strictest regulations are shown in Table 1 below [5].

Table 1: Noise Regulations per country

Requirement	Germany	The Netherlands	Denmark
Sound Exposure Level (SEL)	Max. $SEL_{5\%}$ is 160 dB at 750m distance. Max. $L_{z\text{-}p}$ is 190 dB at 750m distance	Max. SEL level between 163 and 175 dB at 750m depending on season and number of piles.	Cumulative SEL level of max. 183 dB

In order to comply to these regulations noise mitigation measures must be taken. Existing noise mitigation methods are an air-bubble curtain, a noise mitigation screen, a dewatered cofferdam and hydro sound dampers. Deploying these mitigation measures requires additional equipment and increases the complexity of the installation procedure. As a result the risk of delays and the overall installation time is increased. Noise mitigation costs can therefore add an extra €15M to €36M to the installation of the foundation piles of an offshore windfarm, which is a 15% increase of the total installation cost of the foundations [3].

1.1.2. Penetration speed

The rate at which the pile is hammered into the ground is an important factor in the overall installation time. With a hydraulic hammer, piles can be installed in 2 to 3 hours to a penetration depth of 30 to 40 meters. This gives a penetration speed of around 0.5 centimeters per second. An increase of the penetration speed can directly be translated in a reduction in cost since every day at sea costs in the order of a 250.000 euros [6].

1.1.3. Handling time

The installation of a foundation pile includes, in chronological order, the lifting of the pile, placing it in the gripper frame, detaching the crane hook, lifting the hammer, placing the hammer onto the pile, piling operations and the retrieval of the hammer onto the deck. This is a time consuming operation, where a decrease in time again directly translates into a cost reduction.

1.1.4. Fatigue damage

High impact loads of the hydraulic hammer will lead to high fluctuating stress in the foundation pile and therefore fatigue damage. A fatigue damage of 10% to up 20% of the fatigue lifetime can be inflicted during installation. Piles are therefore designed to withstand these high impact loads. This overdesign is found especially in the upper section of the pile, which is the flange on which the impact of the hammer takes place.

1.1.5. Increasing size of foundations piles

The offshore wind industry is striving for a reduction for offshore wind turbines. The power harnessed from the wind scales exponentially with the rotor diameter. Larger wind turbines are therefore more effective and reduce the cost per kWh.

However, larger turbines require larger foundations, which in turn requires larger hammers for installation. The largest diameter monopile that manufacturers can construct is 11 meters. With the current scaling rate this limit is estimated to be reached in 2023. Besides the diameter of the foundation pile, weight is also a limiting factor. The foundation pile is the heaviest component of a wind turbine, the limit of the lifting capacity of most installation vessels is already being reached. Contractors are therefore expanding the lift capacity of their vessels. The Aeolus of Van Oord is being refitted with a 1,600 mT crane and Boskalis is constructing a vessel with a crane capacity of 3,000 mT.

1.2. Proposed solution – The Vibro-drill

The proposed solution to above mentioned problems of noise, time, fatigue damage and the capability of hammering ever larger foundation pile is the Vibro-drill.

The Vibro-drill is a machine that is attached at the tip of the foundation pile and consists of a number of vibrating elements. An artist impression of the machine attached underneath a wind turbine foundation is shown in Figure 1 below. This machine reduces the soil resistance to driving to such an extent that the pile penetrates the soil to the target depth under its own weight. The vibrations at the tip of the pile weakens the soil and displaces it outwards from underneath the pile tip. Water is also injected upwards from the elements to lubricate the pile shaft during installation. After the foundation pile has reached its target depth, the Vibro-drill remains in the ground and can potentially be used to extract the pile during decommissioning phase.

The hypothesis is that without hammering no fatigue damage is inflicted on the pile during installation. Also very little underwater noise will be produced since the little vibrations generated by the Vibro-drill occur underground. The installation process can be simplified due to the reduction in equipment and handling steps. With the modular design of the Vibro-drill simply more elements can be added to accommodate for larger diameter foundation piles.

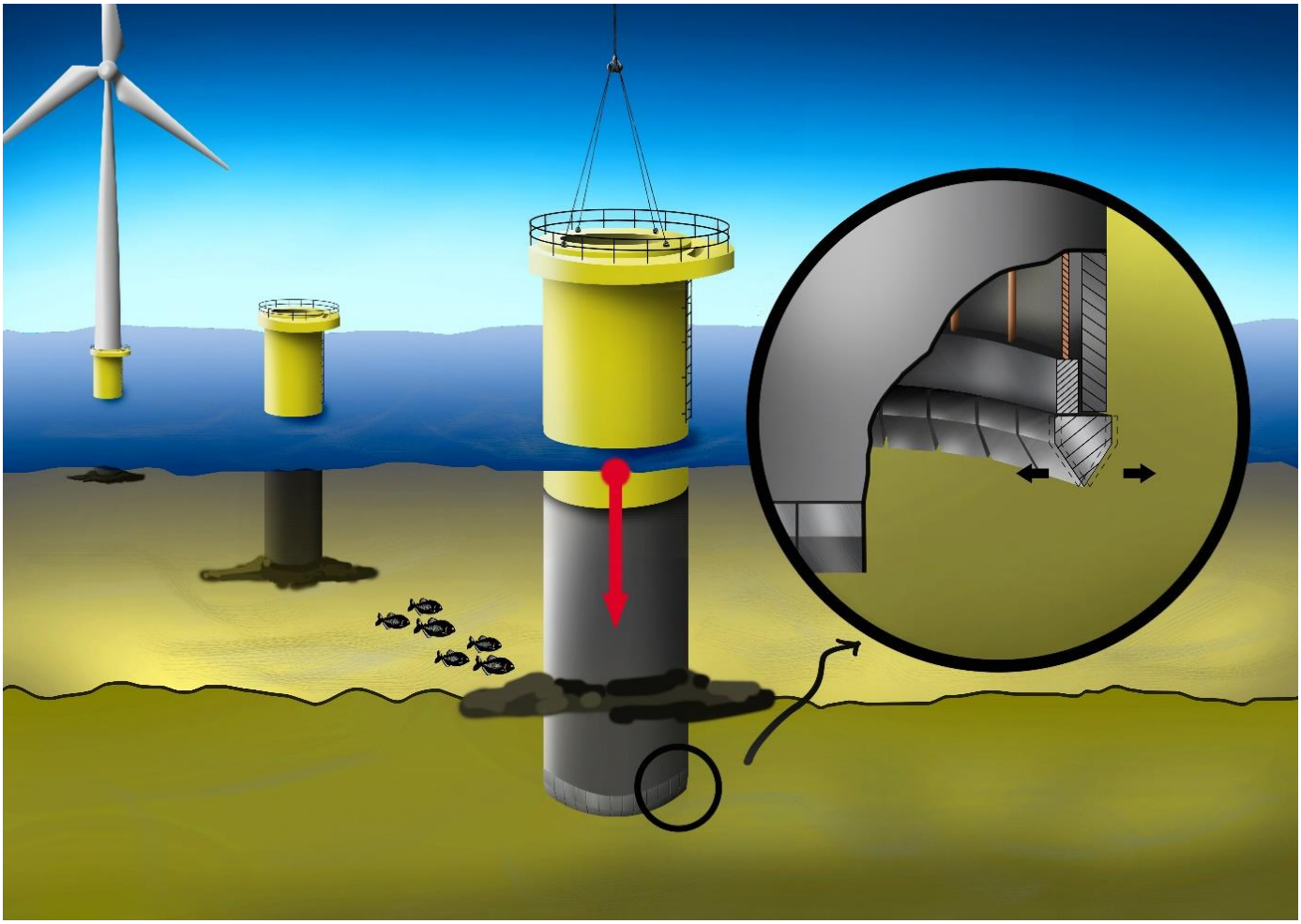

Figure 1: Artist impression of the GBM Vibro-dril

1.3. Aim of the research

The aim of this research is to investigate the feasibility of the Vibro-drill. The feasibility can be split into two parts. The first part is the technical feasibility. The technical feasibility comprises the installation capacity of the pile with the Vibro-drill and the bearing capacity of the pile after installation. The research will focus on this aspect of the feasibility. The second part is the commercial feasibility and whether the proposed solution is indeed a viable solution for the contractors to the described problems. The research will not focus on this part but a discussion is given in the conclusion.

1.3.1. Technical feasibility

The technical feasibility comprises the penetration capacity of the Vibro-drill due to the reduction of soil resistance and the bearing capacity after installation. The vibrations will be generated by a rotating eccentric mass, creating an eccentric force. The effectiveness of the vibrations underneath the pile and the lubrication of the pile shaft will be determined with experiments in which the following input parameters will be varied:

a) Amplitude of eccentric force
b) Frequency of the eccentric force
c) Flow of the lubrication liquid, which will be seawater

Based on the experiments a model will be made to gain a further understanding in the variations of the input parameters and their effects on the penetration capacity.

The bearing capacity after installation will also be determined with experiments. The leading design requirement for the foundation of an offshore wind turbine is the lateral bearing capacity. Therefore, this research will be limited to the lateral bearing capacity and will not incorporate the axial bearing capacity. Furthermore, the axial bearing capacity of foundation piles for offshore wind turbines is estimated to be over dimensioned by tenfold[7].

1.3.2. Technical feasibility

Whether the Vibro-drill is a viable alternative for the current pile driving techniques depends on the technical feasibility and the degree in which it is indeed a solution to the described problems. The following questions concerning the commercial feasibility will be touched upon in the experiments and discussed in the conclusion of this research in section 8.1.

1. Can the Vibro-drill decrease the Sound Exposure Level (SEL)?
2. Can the Vibro-drill increase the penetration speed of the foundation pile?
3. Can the Vibro-drill decrease the handling time?
4. Can the Vibro-drill decrease the fatigue damage in the pile during installation?
5. Can the Vibro-drill decrease the mass of the foundation pile due to a simpler design?

1.4. Approach

There is no prior experience known by the author with an installation method similar to the proposed Vibro-drill. A novelty search performed by an independent patent bureau confirmed that there is no prior art. Therefore, a patent application has been filed. A scaled prototype is constructed to conduct experiments which will be used to determine the technical feasibility, described in section 1.3.1. The commercial feasibility will be discussed in the conclusion and argued with the results of the technical feasibility study.

The prototype has the following settings and functionality. The eccentric force is created by rotating an unbalanced mass; the eccentric mass. The amplitude of the eccentric force is varied by varying the eccentric moment of the mass and by varying the rotational speed of the eccentric mass. The frequency of the eccentric force is determined by the rotational speed of the eccentric mass.

The prototype will be fitted with sensors which will be used to determine the technical feasibility and to validate and verify the penetration model. The sensors measure accelerations, velocities, displacements, forces and flow characteristics.

A penetration model is made to predict the penetration of the prototype and to optimize the Vibro-drill settings for future experiments. The penetration model will be calibrated with the results of the experiments with the prototype.

1.5. Outline

In the second chapter current technologies to install offshore foundation piles are explained. In Chapter 3 the working principles of the Vibro-drill are elaborated upon. The method to study the performance and the description of the prototype is given in chapter four. In the fifth chapter the results of the experiments are given. The penetration model is deducted from basic physical principles and the results of the experiments and discussed in chapter six. In the next chapter the model will be calibrated and validated with the experiments. The final chapter will answer the research questions stated in the section 1.3 together with the recommendations for future work.

2. Offshore Pile Driving Techniques

In this chapter existing offshore pile driving techniques are discussed. Currently, the majority of offshore foundation piles are driven with a hydraulic impact hammer positioned at the head of the pile. Vibratory hammers are also used but less frequent than impact hammers. A new technology called Blue Piling is under development. Also an analysis is given on the performance of each technique. This analysis will use the same criteria as in the commercial- and technical feasibility, described in section 1.3.1 and **Error! R eference source not found.**.

2.1. Impact driving

To date, most offshore foundation piles are impact driven. During impact driving, the hydraulic hammer shown in Figure 2 below, delivers a series of blows to the head of the pile [8], forcing the pile to gradually progress into the sediment. *"The installation of a monopile can last up to several hours depending upon pile dimensions, soil conditions and input energy of the hydraulic hammer. Usually it requires hundreds, if not thousands, of hammer strikes to install a single pile."*[4].

Figure 2: Impact driving with a hydraulic hammer at the Riffgat project [4]

In the problem description, the downsides of impact driving are given. However, there are also a number of advantages associated with impact driving. First of all the piling is a very reliable method. There is very little risk that the pile will not reach the target depth. Also the hammer itself is a reliable. Furthermore, due to the extensive experience with the impact hammer quite accurate installation prediction models exist. For a contractor this reliability is an important argument to use an impact hammer for the installation of foundation piles.

2.2. Vibratory driving

Vibratory driving of foundation piles is done with a vibratory hammer. The working principles of vibratory driving is to reduce the soil resistance to penetration by imparting longitudinal vibratory motions to the pile. Together with a relatively small surcharge force the pile is driven into the ground[9]. The longitudinal motions are generated by rotating eccentric masses inside the vibratory hammer. The vibratory hammer is fixated to the pile with one or more clamps. The benifits of vibratory driving are the high penetration speeds and low noise installation[10]. Also the handling time can be reduced since the internal lifting tool and the

vibratory hammer can be combined in one tool. The fatigue damage to the pile is also considerably less due to the lower stresses in the pile during driving.

Vibratory hammers are not the industry standard because the method lacks reliability on certain aspects. These aspects are the penetration capability and the lateral bearing capacity. On a number of occasions the technique has been used to drive large offshore monopiles, for example the the Anholt OWF [7] and Riffgat OWF [11], of which the vibratory hammer is shown in Figure 3 below. An impact hammer was still necessary to drive the piles to the full target depth. The installation performance vibratory hammers and the bearing capacity of a vibratory driven pile for offshore use is being investigated by several parties. An example of this are the large scale tests performed near Cuxhaven in 2016 [12].

Figure 3: Vibratory hammer used for the Riffgat offshore windfarm project [11].

2.3. Blue Piling

Another new technology under development for the driving of offshore foundations piles is called ‘Blue Piling’. Blue piling is a technology making use of a large water column and a gas explosion to generate the driving force. The technique is described in Figure 4 below.

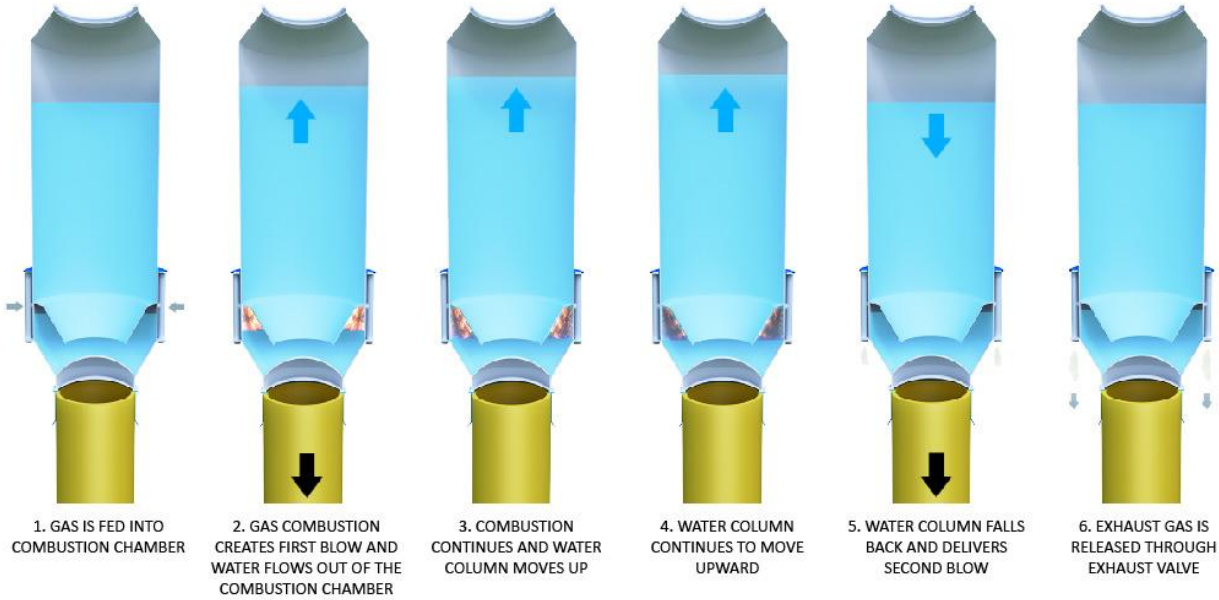

Figure 4: Working principles of Blue Piling, source: www.fistuca.com

Advantages of this technique are lower noise emissions, a gradual force build-up, a low tension stress and also cost-effectiveness. Reduced propagation velocity of the lateral extension of the pile should not only decrease the underwater noise emissions but also the seismic component of radiated noise which is often limiting external noise mitigation systems[2]. Near shore tests with a prototype and a closed end pile with a diameter of 0.66 meter and an open ended pile of 2.25 meters have been conducted. A full scale test is planned in early 2018.

2.4. Summary of the performance of pile driving techniques

A summary of the performance of the three pile driving methods described in this chapter is given in Table 2 below. The scores given to the vibratory hammer and blue piling hammer are relative to the impact hammer which is used as a base case. The Blue Piling method is not yet on the market. Therefore, information on certain topics is not available. The scores given for the Blue Piling hammer are based on information of the website of Fistuca.

Table 2: Performance of pile driving techniques

Criteria	Impact hammer	Vibratory hammer	Blue Piling hammer
Sound Exposure level (SEL)	-	+	+
Penetration speed	+/-	+	+
Handling time	-	+	N/A
Fatigue damage	-	+	+
Reduction in mass	-	+	+
Penetration capability	+	-	N/A
Lateral bearing capacity	+	-	N/A

3. Working principles of the Vibro-drill

In this section the working principles of the Vibro-drill are explained. As mentioned in section 1.2 the Vibro-drill reduces the soil resistance to driving to such an extent that the pile penetrates the soil to the target depth under its own weight. The vibrations at the tip of the pile weaken the soil and displaces it outwards from underneath the pile tip. Water is also injected upwards from the elements to lubricate the pile shaft during installation.

To drive a pile into the soil, the downward force should exceed the upward force, which is the soil resistance to driving. The soil resistance to driving is commonly expressed in two factors; the tip resistance and the shaft resistance[13]. Current pile driving techniques, mentioned in Chapter 2 above, predominantly increase the downward force but also decrease the soil resistance for vibratory driving as described by [14]; *"Soil resistance degrades upon cyclic shearing mainly because of fatigue of the soil skeleton in cohesive soils (Vucetic, 1992), and of effective stress reduction in granular soils (Casagrande, 1938). The effective stress can be ultimately reduced to nearly zero, at which point the soil behaves in a fluid-like manner."*

The working principles of the Vibro-drill are to decrease the soil resistance to driving to a value below that of the pile weight, enabling a penetration into the soil without an additional downward force. The tip resistance and shaft resistance are decreased in two different ways described below.

3.1. Reduction of shaft resistance during pile driving

The reduction of the shaft resistance is achieved by jetting water upwards along the pile shaft from the bottom end. This will form a boundary layer of upwards flowing water between the pile shaft and the surrounding soil. If a full boundary layer is formed, the remaining shaft resistance will be that of the flowing water around the pile shaft. This resistance is assumed negligible.

A second function of the water injection will be that of transporting soil particles upwards, maintaining the boundary layer and preventing soil particles to clutter around the pile shaft. A flow speed that exceeds the terminal velocity of a soil particle should at least be maintained. The flow is considered laminar with a low Reynolds number of under 0.2, called a Stokes flow. The terminal velocity of a sphere in a Stokes flow is calculated with[15]:

$$v = \frac{d^2 g(\rho_s - \rho_f)}{18\mu}$$

Where

μ	is the viscosity of the medium
d	is the diameter of the soil particle
ρ_s	is the density of the soil
ρ_f	is the density of the medium

A flow speed that exceeds the terminal velocity of the soil particles will transport any soil particles, within this certain diameter range, in the boundary layer upwards and out of the boundary layer, keeping the friction low. The flow speed should not be too high. In this case large quantities of soil could be transported to the surface creating a large gap between the pile and surrounding soil, negatively affecting the bearing capacity of the pile. Experiments with the prototype pile will be conducted to measure the lateral bearing capacity.

3.2. Reduction of tip resistance during pile driving

The reduction of the tip resistance is achieved by weakening the soil with vibrations and displacing the soil from underneath the tip of the pile outwards to the surrounding soil. Due to this displacement the soil will also be compressed around the pile tip. This creates a 'free' space into which the pile can penetrate. The displacement of the soil is achieved by the oscillating motions of elements of the Vibro-drill. The amplitude and frequency of the oscillations will be of influence to the effectiveness of weakening of displacing the soil.

The magnitude of the oscillations causes a certain cyclic load τ_{cyc} onto the soil. An estimate of the magnitude of this load is attempted to find for the design of the prototype. By dividing the load with the average stress s_{uss} the cyclic load ratio is calculated. Randolph and Gouverec (2011) identified the cyclic load ratio as a very important factor for the bearing capacity of soils when subjected to cyclic loading. As an example Figure 5 shows the strain percentage, γ, for a given cyclic load ratio over a number of cycles. For a high load ratio very little cycles are required to produce a shear strain of 15%, vice versa, for a high number of loading cycles a lower cyclic load ratio can be applied to achieve the same shear strain.

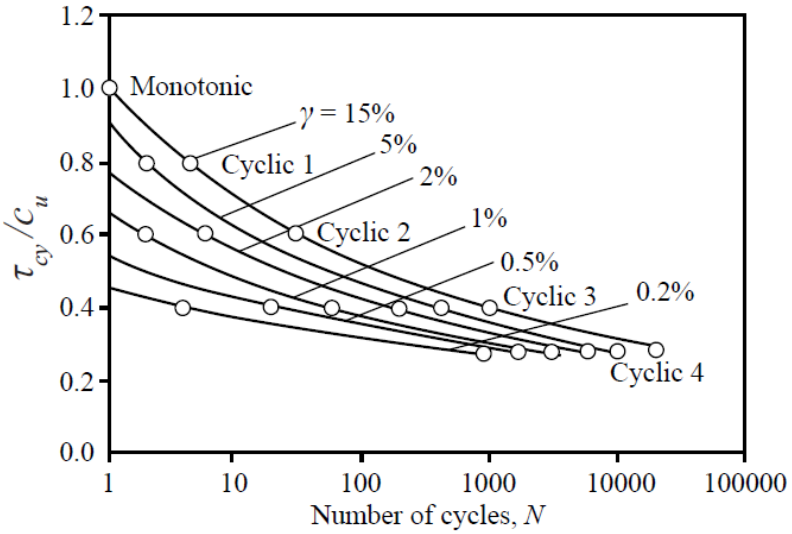

Figure 5: Strain contour diagram of sand. Average shear stress equal to zero. (Randolph and Gouverec) [16]

The cyclic behavior is not governed by the maximum shear stress but by the amplitude of the cyclic load. Research conducted by [17] shows the effect of the maximum shear stress and the amplitude of the cyclic load ratio, shown in Figure 6 below. The soil in the test with an average shear stress $\tau_a = 0$ and a maximum cyclic load amplitude of 50 kPa fails after 10 cycles, whereas the test with $\tau_a = 0.5\tau_{max}$ and $\tau_a = 0.85\tau_{max}$ have developed only small shear strains after 2500 and the test with the highest τ_a has the smallest shear strains.

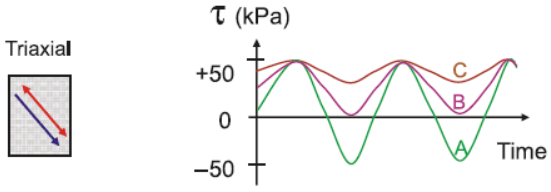

Test	τ_{max}	τ_a	τ_{cy}	Result
A	50	0	50	Failure (γ = 15%) 10 cycles
B	50	25	25	γ_p = 0.8%, γ_{cy} = 0.3% 2500 cycles
C	50	42.5	7.5	γ_p = 0.03%, γ_{cy} = 0.02% 2500 cycles

Figure 6: Results from cyclic triaxial tests with the same maximum shear stress.[17]

This behavior is explained with a decreasing Secant Shear modulus over a number of cycles. In Figure 7 below the Secant Shear Modulus (G_s) decreases with every loading cycle. The curve that represents the initial loading is referred to as the initial 'backbone' curve, because it also serves as the basis to generate the family of curves corresponding to unloading and reloading. The energy contained in a loop depends on the soil conditions and the amplitude of the cyclic strain.

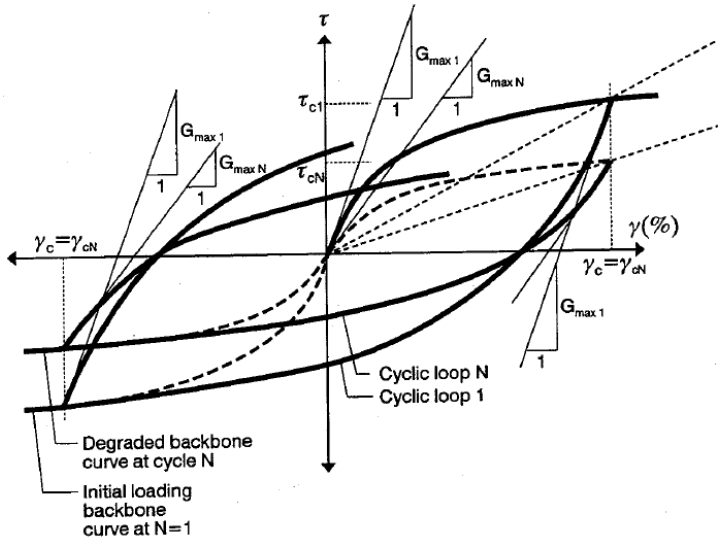

Figure 7: Soil behavior under constant cyclic shear strain amplitude loading (From Vucetic 1993; 1994) [14]

The decrease of the secant shear modulus is explained with an increase in pore water pressure due to the cyclic loading and a continuously deterioration of the soil structure [18].

3.3. Discussion

Considering the working principles a design of the prototype is made. The prototype should include upwards water injection and one or multiple vibrating elements at the bottom end of the pile. The abovementioned soil reactions to cyclic loading are mostly qualitative descriptions. Soil is a very irregular medium which also changes properties when subjected to loadings and deformations. To model the physical soil response to cyclic loading and the subsequent elastic- and plastic deformations is near to impossible.

Therefore, experiments will be conducted to determine the effectiveness and the optimal properties of the vibrations and the lubrication layer. Also the lateral bearing capacity is investigated with experiments and compared to an industry standard bearing capacity model for impact driven piles.

The experimental setup and the prototype of the Vibro-drill is described in the next section.

4. Experimental setup

A scaled prototype of the Vibro-drill is constructed and tested multiple times on Maasvlakte II in the Port of Rotterdam. The experimental setup of the prototype and the measurements during the experiments are described in this chapter.

4.1. Prototype description

In this section the design choices and the design of the prototype are given. How the prototype relates to the Vibro-drill and which considerations play a role in design is also explained.

4.1.1. Translating the Vibro-drill to a representative prototype

The Vibro-drill consists of a ring of identical elements attached to the bottom end of the foundation pile shown in Figure 8 below. On the left the bottom view is shown, on the right a cross-section over the length of the bottom part of the pile. The elements have wedge shaped tips that will displace the soil to either side of this wedge. The width of the elements indicated in the bottom view will be slightly larger than the wall thickness of the foundation pile to create the gap for the lubrication layer. The diameter of the pile is 50 to a 100 times larger than the width of the elements. Therefore, it is unlikely that the soil and motions of the elements on the opposite side of the foundation pile will be affected by the other side. A prototype that comprises an entire ring of vibrating elements is for this reason deemed unnecessary and a single element prototype is chosen.

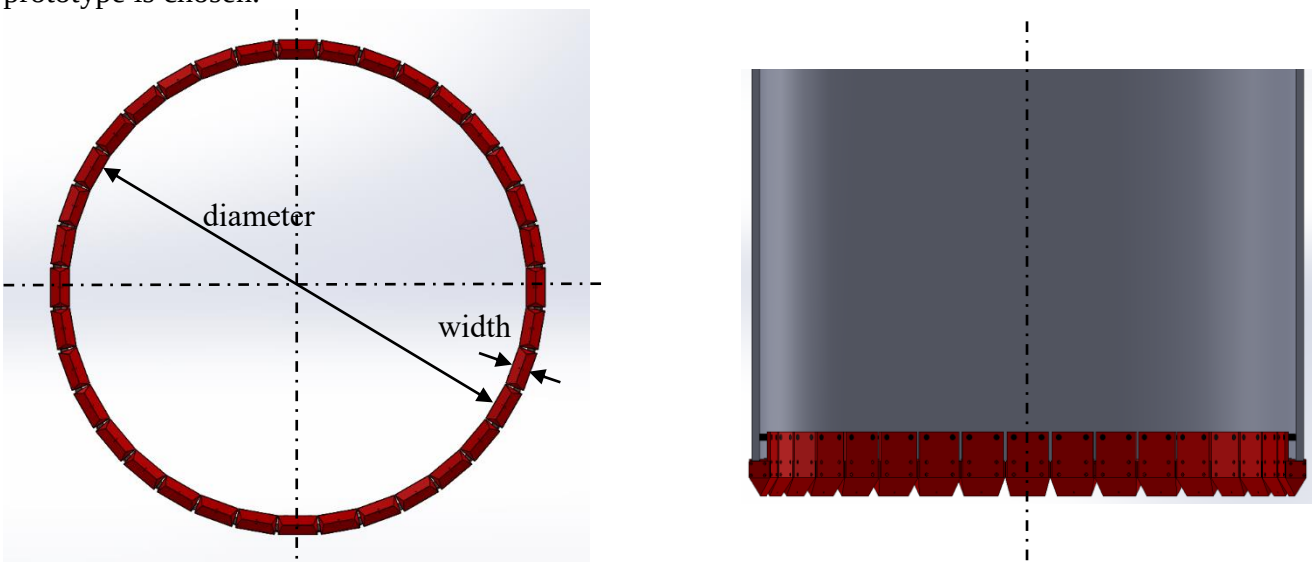

Figure 8: Schematic of the Vibro-drill attached to the bottom end of the foundation pile

Constructing and testing only one vibrating wedge shaped element poses a number of challenges. If a wedge shaped tip is used the prototype will not will be symmetric around vertical axis. This would lead to more complex dynamic behavior. The construction, assembly and design would also be more complex and expensive. Also the penetration model would have to incorporate more variables, leading to a model which is harder to calibrate and will therefore be less reliable.

An axis-symmetric conical shaped tip is therefore chosen as a prototype for the Vibro-drill. The tip is attached to a steel pile with a slightly smaller diameter to create the gap for the lubrication layer. In the next section the design and construction of the prototype is explained.

4.1.2. Design of the prototype

The technical feasibility that will be investigated in this research will cover the penetration capacity and the lateral bearing capacity of the installed pile. The dimensions and properties of the prototype will determine the available test range. These dimensions are the length of the pile, the diameter of the pile and tip and the range of amplitudes and frequencies of the excitation force.

Vibrating element

The vibrations are excited by a rotating eccentric mass inside the conical tip, powered by a hydraulic motor. The main design choice for the hydraulic motor was the highest possible rotational speed to extend the test range as far as possible. Three eccentric masses with different eccentric moments are constructed to test the influence of different loading amplitudes for a given frequency. The loading amplitude is calculated with the following formula:

$$F = me\omega^2$$

Where

- m is the total mass of the eccentric mass
- e is the eccentricity which is, the distance between the center of gravity of the eccentric mass and the axis of rotation
- ω is the rotational speed of the mass

The eccentricity multiplied with the total mass is called the eccentric moment. The eccentric moment is created by removing material on one side of a cylinder, illustrated in Figure 9 below.

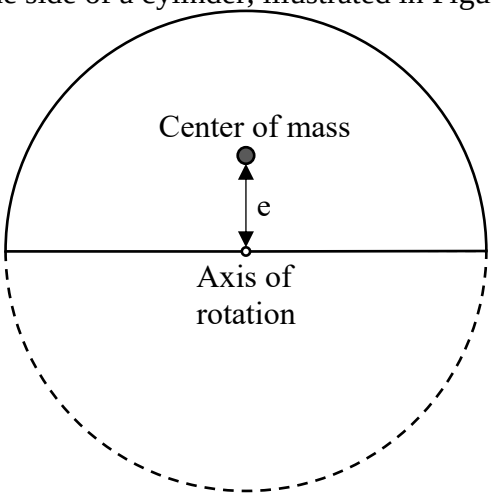

Figure 9: creating the eccentric mass

Water injection

The water injection system consists of four water lines for an even spread, that eject the water upwards from an opening between the pile and the element. This flow of water forms the lubrication layer between the pile wall and the surrounding soil during installation.

Sensors

The prototype was fitted with a number of sensors to measure the penetration depth, pressure and flow to the hydraulic motor, pressure and flow of the water injection, accelerations of the vibrations and the pull-down force on the pile.

Pile

The pile used for the prototype has a length of 5 meters. This length was chosen as the maximum length possible to mount onto the existing piling rig. The largest possible length is desirable in order to test the prototype to the largest possible depth.

Based on these design considerations a prototype of a single vibrating element, shown in Figure 10 and Figure 11 below, has been constructed. In Figure 12 below the prototype attached to the piling rig is shown with the location of the sensors. In Appendix C – Sensors a more detailed explanation of the sensors is given.

In Appendix B – Prototype design, fabrication and construction a more detailed explanation of the design and construction of the prototype is given.

Figure 10: Vibrating element attached to the foundation pile.

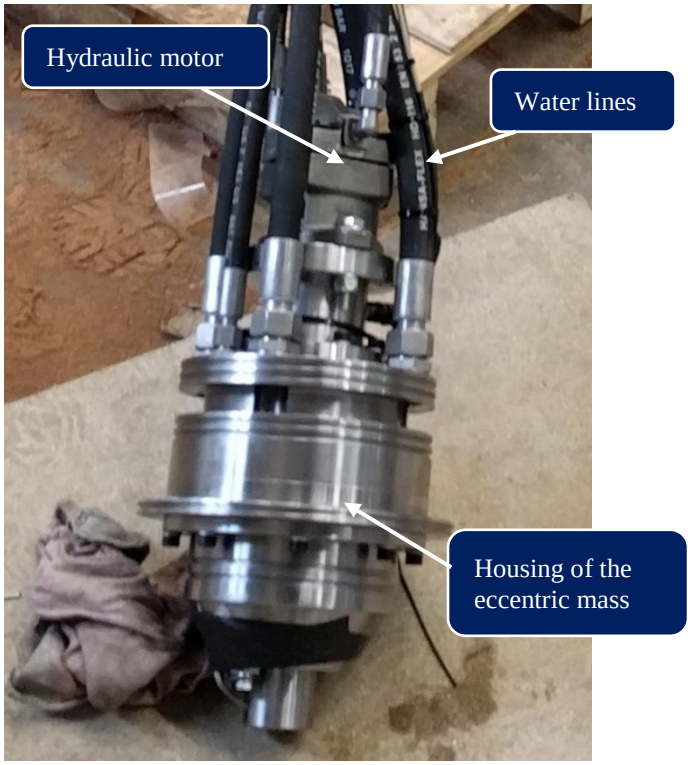

Figure 11:Inner parts of the vibrating element

In section 4.5 the scale factors of the prototype to the Vibro-drill are explained and how these factors influence the feasibility study.

Figure 12: Prototype of the vibro-drill

4.2. Penetration tests

The penetration tests with the prototype will be conducted on a grid of 35 meters by 25 meters. A new location will be used within this grid for every test. The minimum distance between the tests will be 3 meters to minimize the influence between tests. An overview of the test locations is given in Appendix D – Location of experiments and soil conditions.

4.2.1. Variation of test parameters

A variation of 3 eccentric masses and 3 rotational speeds, giving 9 different configurations will be tested. The configurations are shown in Table 3 below. The maximum penetration depth is 4.5 meters, limited by the length of the pile.

Table 3 Planned test scheme:

Number of tests per variable		**Rotational speed [RPM]**		
		4000	**8000**	**12000**
Eccentric	*0.005*	5	5	5
moment	*0.010*	5	5	5
[kgm]	*0.015*	5	5	5

4.2.2. Measurements

Several parameters were measured to determine the effectiveness of the prototype and to verify and validate the penetration model. Below in Table 4 the measured quantities are listed.

Table 4: Measured quantities during the experiments

Parameter	**Sensor**	**Comment**
Rotational speed of eccentric mass and motor	Hydraulic flow and pressure sensor	The hydraulic motor displaces 4,9 cc per revolution.
Power of the motor	Hydraulic flow and pressure sensor	The hydraulic power is flow rate times pressure.
Penetration depth over time	Pulse wheel	Per meter the wheel gave 200 electric pulses.
Accelerations in the vibrating element	Accelerometer	Acceleration are measured in all three directions.
Downward force on the pile	Loadcell	The loadcell is attached to the winch cable
Water flow and pressure	Water flow and pressure sensor	

The maximum rotational speed of the motor is 200 revolutions per second. The Nyquist-frequency is two times the highest frequency, which dictates a sampling rate of 400 Hz. For redundancy the sampling rate was set to 1000 Hz.

4.3. Lateral bearing capacity tests

Lateral bearing capacity tests are conducted. The pile is tested multiple times with different settle times. The results and a more detailed test description are shown in section 5.5.

4.4. Test location and soil measurements

The Maasvlakte II was chosen as a test site because it is constructed with sand from the North Sea[19], the area of application for the Vibro-drill. The specific test site has been compacted with the use of compaction machines. This gave us a compact upper soil layer to test our prototype. At the test location Cone Penetration Tests (CPT) are taken. A total of five measurements are conducted equally spread over the test area. The data of these measurements is used as input for the penetration model and to determine the stiffness of the soil and the type of soil. A more detailed description and the results of the CPT are given in Appendix A – Soil at test location.

4.5. Scale factors

The prototype is a scaled version and an approximation to the Vibro-drill. Three governing scale issues are identified, two of which concern the prototype and one concerns the soil condition. For the prototype these are the distance of the soil displacement and the total depth of installation. The soil conditions in which the installation takes place dictates the effort it takes to displace and liquefy the soil. The scale factors are elaborated upon in this section and a summary is given in Table 5 below.

4.5.1. Distance of soil displacement

The ability of the vibrating elements to displace and weaken the soil over a certain distance is of vital importance. It is assumed that the soil is mostly compressed when displaced by the vibrating elements. The required load to compress soil over a certain distance increases with the total compressed distance. In other words, a displacement of 0 to 10 mm requires a much lower load than a displacement from 90 to 100 mm. A relationship for the required load and the resulting compression is given by[20] and is called the logarithmic compression law of Terzaghi:

$$\epsilon = -\frac{1}{C_2}\ln\left(\frac{\sigma}{\sigma_1}\right)$$

Where

- ϵ is the compression
- σ is the applied load
- σ_1 is the load at the start without deformation
- C_2 is a compression constant depending on the type of soil

Monopiles have a typical wall thickness of 70 to 100 millimeters. The Vibro-drill will be a little wider with 150 millimeters. The soil is pushed to both sides over a distance of 75 millimeters. The prototype displaces the soil over a maximum distance of half the diameter of the tip, which is 135 millimeters. The soil displacement with the prototype is actually larger than necessary with the Vibro-drill. This gives extra confidence in the capability of the Vibro-drill to displace the soil.

4.5.2. Penetration depth

Depth is an important factor because the pressure increases with increasing depth. This has an effect on the effort it takes to displace and weaken the soil. The depth to which the prototype pile penetrated is 4.5 meters. A monopile is typically installed to a depth of 30 to 40 meters. Further experiments will be necessary to determine the penetration capacity to this installation depth.

4.5.3. Soil conditions

The resistance of soil also penetration depends on the strength of the soil through which the pile has to advance. The strength of the soil is commonly measured with a Cone Penetration Test. A cone attached to a long rod is pushed through the soil while measuring the resistance at the tip and the friction along the shaft. The tip resistance is a parameter for the effort it takes to compress and/or displace the soil. At the test site cone resistances of up to 30 MPa were measured within the test depth range. In the North Sea, where the monopiles are installed to up to 45 meters depth, cone resistances of up to 100 MPa can occur.

Table 5: Scale factors of the prototype to the Vibro-drill

Dimension	Prototype	Monopile	Scale factor
Soil compression distance [m]	135	75	1.6:1
Soil conditions - cone resistance [MPa]	30	100	1:3.3
Penetration depth [m]	4,5	35 - 45	1:8 – 1:10

5. Results of experiments

The results of the experiments are given in this chapter. These include the penetration tests, the lateral bearing capacity tests, sound measurements and stress calculations. The experiments on Maasvlakte II show that soil penetration with this prototype is possible. The three eccentric mass configurations were tested. However the intended variation of the rotational speed, as described in Chapter 4, of the eccentric mass could not be realized. Below in Table 6 a summary of the experiments is given with the average performances per eccentric mass configuration.

Table 6: Summary of experiment results

Eccentric mass configuration	Eccentric moment [kgm]	Average penetration speed [mm/s]	Average rotational speed during tests [rad/s]	Average motor power [kW]	Average eccentric force [kN]
Small	0.005	3.10	1,200	19.5	7.20
Medium	0.010	23.0	1,100	23.5	12.1
Large	0.015	18.2	840	21.0	10.5

5.1. Analysis of the pile penetration performance

The working principles tested with the prototype are analyzed. The reduction of the shaft resistance due to the water flow and the reduction in tip resistance due to the oscillations are described below.

5.1.1. Reduction of shaft resistance with water flow

The water was injection at a constant flowrate of 200 l/m. During most experiments water was flowing continuously to the surface, indicating a fully developed boundary layer shown in Figure 13 below. The pressure at the water inlet was measured. This pressure never exceeded 1 bar overpressure, indicating a low resistance to flow.

Figure 13: Upwards flow of water forming a lubrication layer between pile shaft and surrounding soil.

In some cases, water ceased to flow. Two site conditions combined could have caused this.

1. The soil type at the Maasvlakte II is sand, which has a high porosity.
2. The experiments were conducted above sea level, allowing the water to flow to the dry surrounding soil.

The area of application is offshore and underwater. Water flowing outwards into the surrounding saturated soil is less likely in this case. However, the large surface area of the shaft of the monopile could cause preference flows in the boundary layer, leaving parts along the shaft unlubricated.

5.1.2. Reduction of tip resistance with oscillation tip

The effectiveness of the reduction of the tip resistance can be derived from the penetration speed of the prototype pile. The effect of the loading amplitude and frequency is analyzed.

Loading amplitude

The order of high to lowest loading amplitude is the same order as the high to lowest average penetration speed. The relation between loading amplitude and penetration speed seems to be a nonlinear one. The small eccentric mass exerts approximately half the force but has a 7 times lower penetration speed.

Loading frequency

The loading frequency doesn't seem to effect the penetration speed directly. The highest loading frequency, applied with the small eccentric mass, shows the lowest average penetration speed.

A combination of a high frequency and high eccentric force seems to be most effective. In combination with the penetration model results, final conclusions on this are drawn in Chapter 8.

5.2. Penetration diagrams of all configurations

In Figure 14 to Figure 16 below the penetration diagrams are shown for the small, medium and large eccentric mass configurations respectively. The lines are colored to indicate the highest to lowest relative average cone resistance at the location the experiment was conducted, from red to green respectively. This indication is given per configuration, i.e. the same color in a different configuration doesn't indicate the same cone resistance. The legend shows the experiment sequence number, in Appendix D – Location of experiments and soil conditions the location of each experiment can be found.

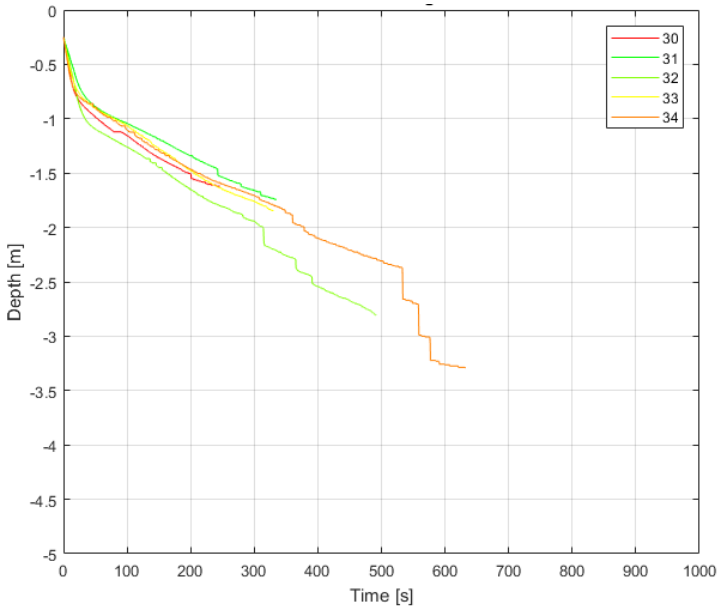

Figure 14: Small eccentric mass configuration penetration diagram

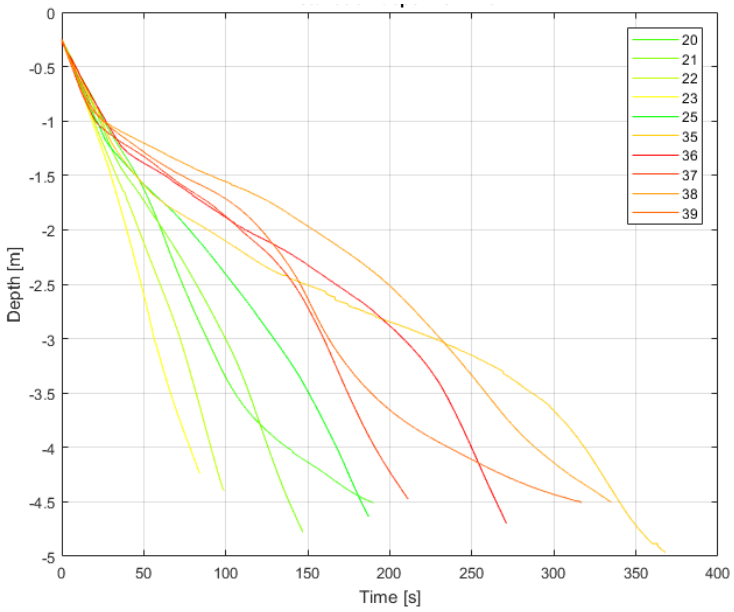

Figure 15: Medium eccentric mass configuration penetration diagram

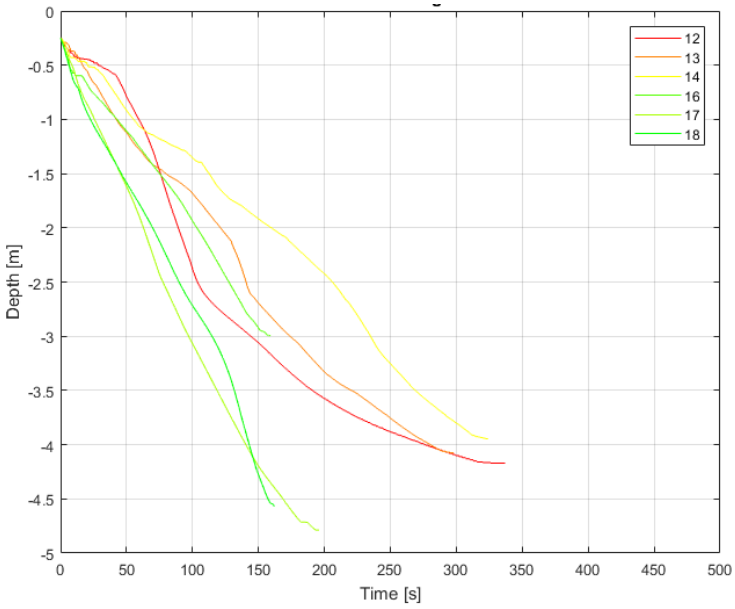

Figure 16: Large eccentric mass configuration penetration diagram

5.3. Discussion of the performance of the prototype

In this section a general discussion is given on the results of the experiments and for each configuration.

Looking at the three penetration diagrams, a positive correlation between the cone resistance and penetration speed can be seen. Especially for the medium eccentric mass configuration this can be seen clearly. The highest penetration speeds occurred in soil with a low cone resistance and vice versa.

The spread on the other hand is largest for the medium eccentric mass configuration with the fastest experiment being 4 times faster than the slowest. The locations of these experiments were more spread out for this configuration, but the CPT measurements do not indicate a very large spread in soil stiffness. Non-linear soil effects probably play a role in this result. The configuration itself might also be more susceptible to a wider range of test results. Looking at the rotational speeds during the experiments, given in section 7.3, also the medium configuration is showing the largest spread.

Other external causes will also have an effect on the penetration speed. Possible causes are identified:

1. (Very) local variations in the stiffness of the soil

2. Rocks
3. Other anomalies such as pieces of wood, cloth etc. are found on the test location.
4. Influence of the order of tests
5. Influence of the number of tests in the direct vicinity

5.3.1. Light weight

Penetration with the light weight configuration was very slow in the first few meters and not possible to 4.5 meters depth. The excitation force is only half compared to the middle and heavy weight configuration. The light weight at the given rotational speeds simply doesn't supply enough force to penetrate deep into the ground.

5.3.2. Middle weight

Penetration of the soil with the middle weight configuration was most successful. The fastest penetration speed was accomplished with this configuration. Looking at the average applied eccentric force, being 12.1 kN, it could explain the highest penetration speed.

5.3.3. Heavy weight

The heavy weight penetrated the soil a bit slower than the middle weight but still very effective. The limiting factor in this configuration was the rotational speed that would not exceed 850 rad/s, probably due to the limited torque of the motor.

5.4. Pile refusal occurrences

On a number of occasions pile refusal occurred, below these and the possible causes are explained.

5.4.1. Refusal at locations with high qc values

Soil measurements of the test site revealed that one area was particularly stiff. Here the cone resistance was above 30 MPa at only a few meters depth. A possible explanation for the refusal of the pile is the density of the soil. If this density exceeds a certain threshold the soil displays dilative behavior upon shearing.

5.4.2. Pile refusal without water injection

A number of installations without water injection were tested. In each case the penetration halted before reaching one meter depth. Based on these results, water lubrication appears to be essential for the penetration capability of the prototype. First of all, without water lubrication the shaft resistance will be much higher. Secondly, the effective pressure of the soil on the pile is higher without water in the soil. The effective stress is a function of the total stress and the water pressure with the following relation:

$$\sigma' = \sigma_{total} - pore\ water\ pressure$$

If no water is injected, the effective stress is higher, making it harder to displace the soil. Furthermore the cyclic load ratio decreases with increasing effective stress. This increases the required number of cycles to compress the soil.

5.5. Lateral bearing capacity tests

Several lateral bearing capacity tests are performed, the set-up is shown in Figure 17 below. The piling rig was adapted to exert a horizontal force on the pile. The loadcell was used to measure the force applied to the pile.

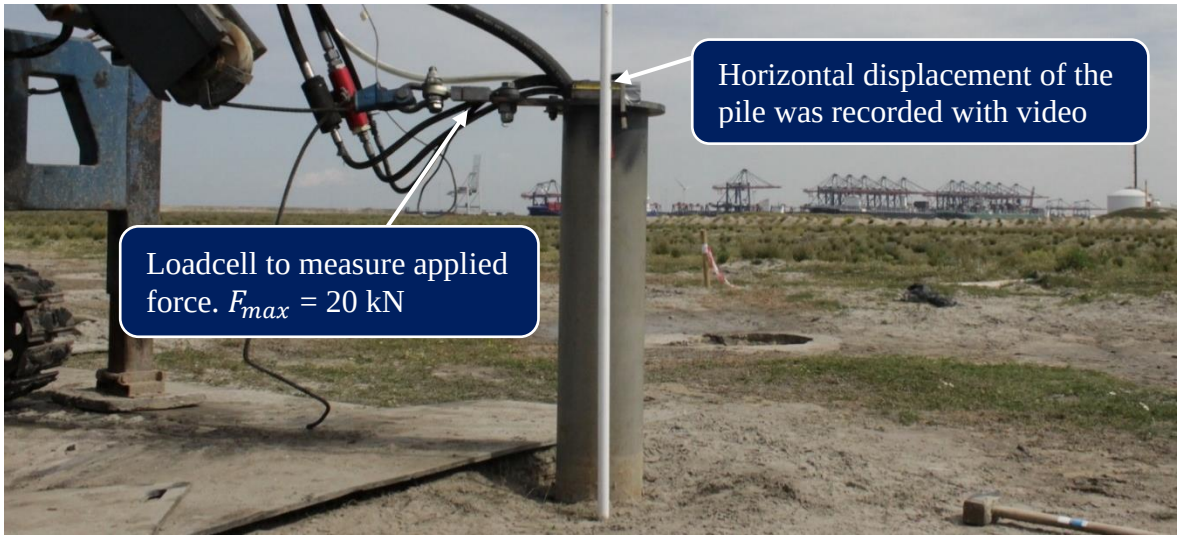

Figure 17: Set-up of lateral bearing capacity test

Test properties:

1. Stickup length of 1,1 meters
2. Penetration depth of 4,3 meters
3. OD of 245 mm, WT of 6,3 mm
4. Applied load of maximum 20 kN

In total eight tests were performed. The amount of time after installation was also varied to see if soil setup had an effect in the lateral bearing capacity. The test results are shown in Table 7 below.

Table 7: Lateral bearing test results

Test #	Number of days after installation	Maximum deflection [mm]
1	2	10
2	2	10
3	1	12
4	1	10
5	1	10
6	0	13
7	0	12
8	0	12

In Figure 18 below the test results are shown together with the modelled deflections. The average deflection of the eight tests was 11 mm, with a standard deviation of 1.16 mm. The piles with the longest setup time show a somewhat higher stiffness. For the modelled deflections the P-y curve method is used[13]. Four different soil inputs are used. Three deflection curves are modelled with an uniform distributed soil and an angle of internal friction of 36, 40 and 45 degrees (green, yellow, red). The soil input for the fourth deflection curve is based on CPT data acquired at the test location (black).

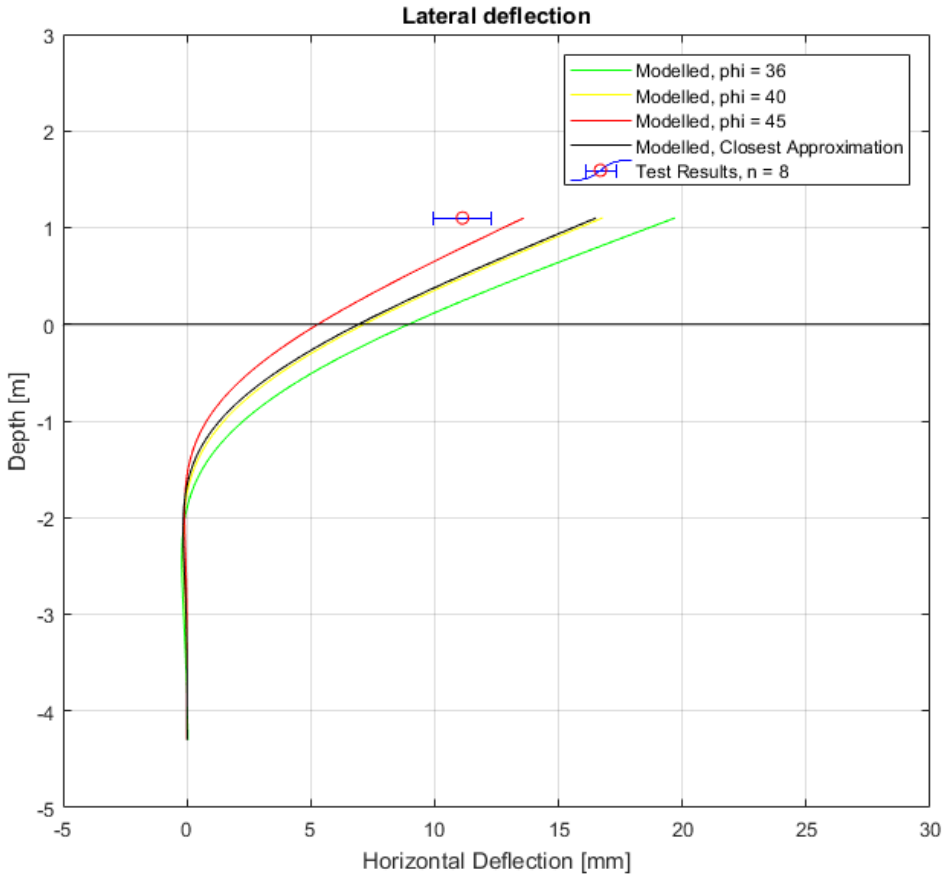

Figure 18: Test results of lateral bearing capacity and modelled deflection curves with P-y curve method

Of the eight tests that were conducted, all showed a higher lateral bearing capacity than the theoretical lateral bearing capacity. This is a very positive test result to gain a degree of confidence in the capability of the new installation method to install a foundation pile which is up to standard. This result was not expected. Due to the reduction of the soil resistance during the installation it was expected that the bearing capacity would also be reduced. However, since this is not the case the most likely reason for this bearing capacity is that the soil is compacted around the pile. This compaction could explain the higher lateral bearing capacity.

5.6. Sound Exposure Level

The harmful noise caused by piling at sea affects life in the water, the tests were performed on land. The measured noise levels during the installation were approximately 89 dB at 5 meters distance. Pile driving of a similar pile on land is on average 110 dB at 5 meters distance.

5.7. Stresses in the pile

Fatigue in a pile during installation with the prototype can occur in two ways; i) due to bending of the pile or ii) due to compression of the pile. In steel, the fatigue limit is typically 0.4 times the ultimate tensile strength. For normal steel the ultimate tensile strength is around 300 MPa. Considering this, if the stress does not exceed 120 MPa no fatigue damage is caused during the tests. The following maximum stresses are calculated:

1. The largest compression force on the pile was 20 kN due to the winch force and its own weight. This force divided by the cross-sectional area of the pile wall gives a stress of 4,2 MPa. This is almost a factor 30 lower than the fatigue limit strength.
2. The highest bending amplitudes recorded where around 1 mm over a pile length of 5 meters. This deformation gives a maximum stress of 2,05 MPa. Which is more than a factor 60 lower than the fatigue limit strength.

6. Penetration model

To predict the penetration speed of the prototype pile into the soil a model is made. The input values of the model are calibrated with the experiment results. First a force equilibrium is set up, with which the magnitude and direction of the resulting force of the prototype onto the soil is determined. The reaction force and subsequent displacements of the soil are modelled in this direction. The geometry of the tip and the direction of the plastic soil displacements are used to calculate the penetration into the soil. For future research and experiments, the model can be used to optimize the prototype properties for future experiments.

6.1. Force equilibrium between soil and prototype

The following forces are working on the pile and illustrated in Figure 19 below.

- F_g is the weight of the pile
- F_{winch} is a force exerted on the pile by a winch in downward, vertical direction.
- $F_{ecc}(t)$ is a force exerted by an eccentric mass in the tip of the pile rotating about the z-axis.
- $F_{soil,shaft}$ is the friction force between the shaft of the pile and the surrounding soil.
- $F_{soil,tan}(t)$ is the tangential reaction force of the soil acting along the tip of the pile
- $F_{soil,norm}(t)$ is the normal reaction force of the soil acting on the tip of the pile.

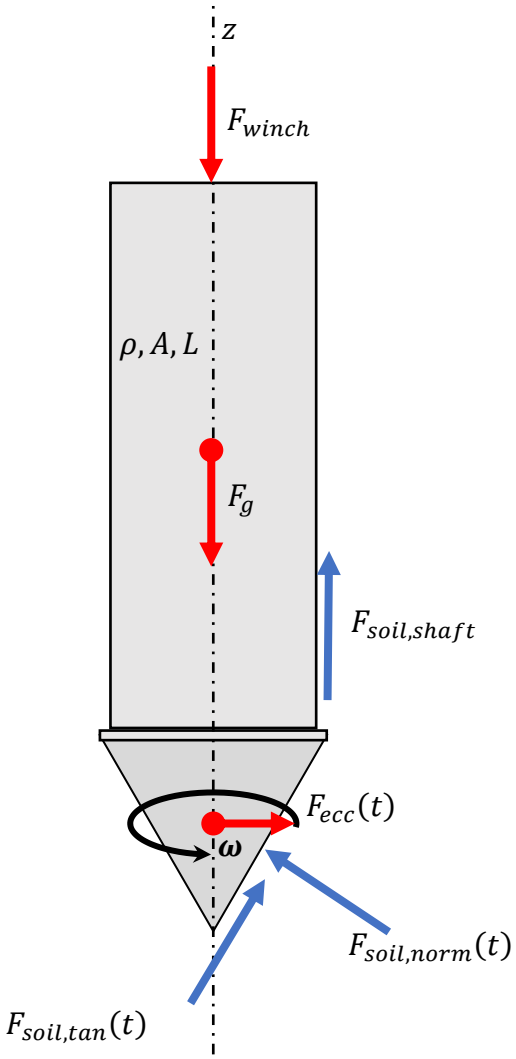

Figure 19: Force equilibrium on prototype pile

The following assumptions are made on the forces acting on the pile:

1. Due to the low friction value of the soil and the water lubrication, the shaft friction force is assumed to be zero.

2. A homogeneous soil is assumed in the horizontal plane, i.e. the soil on the left side of the pile is assumed to have the same characteristics as the soil on the right side of the pile.
3. The winch force is a constant force, forming with the weight of the pile a constant downward force; $F_{push} = F_{winch} + F_g$

With these assumptions a force equilibrium at the pile tip in the x-z plane is given in Figure 20.

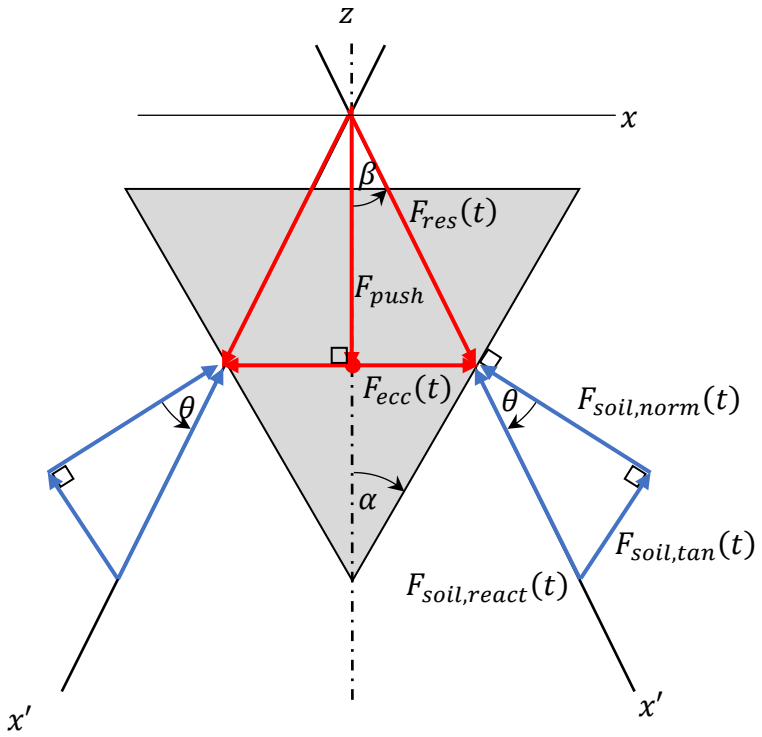

Figure 20: Force equilibrium transposed and decomposed at the tip of the prototype pile

The force equilibrium is displayed on both sides of the tip to emphasize the symmetry about the z-axis. Due to the assumption of a homogeneous soil and the rotation of the eccentric mass about the z-axis they are identical. The resultant soil reaction force is the combined normal and tangential component. The angles are given or calculated with:

$$\alpha = 30^0$$
$$\beta = \tan^{-1}\left(\frac{|F_{ecc}(t)|}{|F_{push}|}\right)$$
$$\theta = 90 - \alpha - \beta$$

The reaction force of the soil along the x'- axis is calculated with:

$$\sum \boldsymbol{F}_{x'} = \mathbf{0};\ F_{push}\cos\beta + F_{ecc}(t)\ \sin\beta + F_{soil,norm}(t)\,cos\,\theta + F_{soil,tan}(t)\sin\theta = 0$$

Where the resultant force acting on the soil is calculated with:

$$F_{res}(t) = F_{push}\cos\beta + me\omega^2\sin(\omega t)\sin\beta$$

6.2. Modelling pile, soil and applied forces

The soil and pile are dynamically modelled with spring, damper and slider elements. In this section an explanation is given of how the soil and pile are modelled.

6.2.1. Soil model

To model the soil, several assumptions are made. First, it is assumed that the response of the soil can be split into two types. Elastic soil behavior which occurs for small strains and plastic soil behavior which occurs for larger strains. The elastic soil behavior is modelled with a Kelvin-Voigt element. The plastic soil behavior is modelled with a slider and damper element. The slider element is incorporated to set a threshold value for which the soil starts to plastically deform. Furthermore it is assumed that the soil is a homogeneous medium and will therefore react similar in all directions.

In the previous section 6.1 the force equilibrium between the pile and soil is given. From this equilibrium a soil reaction force acting in a certain direction was found. The soil reaction force is therefore modelled in the same direction represented by axis x'. Therefore, the plastic- and elastic soil deformations captured in x'_m and x'_f respectively will also occur in this direction. An illustration of the position of the modelled elements with respect to the pile and soil is shown in Figure 21 below.

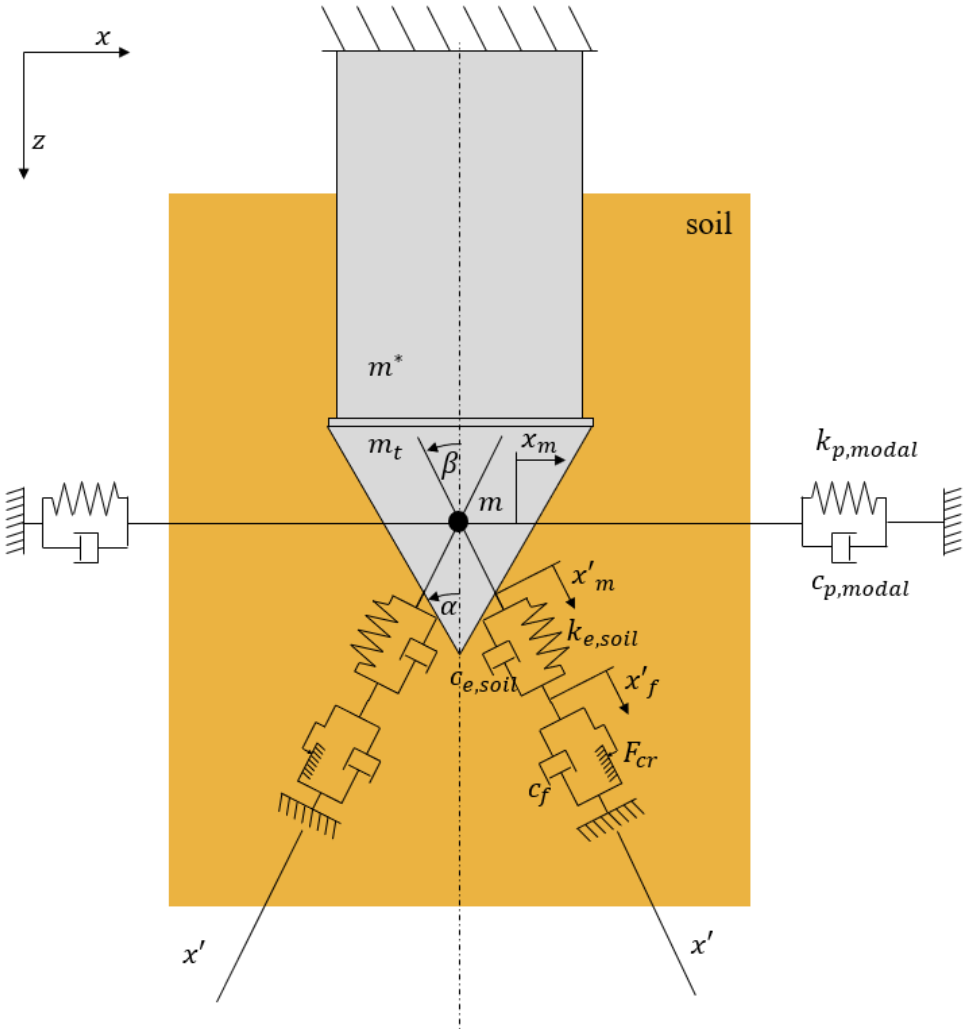

Figure 21: Illustration of soil and pile model

6.2.2. Pile model

The pile is a steel tube with the prototype attached to the bottom end. At the top end the pile is rigidly attached to the piling rig. To capture the modal stiffness $k_{p,modal}$ and damping $C_{p,modal}$ of the pile another

Kelvin-Voigt element is introduced. The modal mass (m^*) of the pile is added to the mass of the tip (m_t) to incorporate in the model as a single point mass.

The assumption of elastic and plastic soil deformation along the x'-axis provides the possibility to model the penetration of the pile into the soil in one dimension. The elements to model the soil are already oriented along this axis. However, the pile modal properties are not. To correctly model the modal mass, -stiffness and -damping of the pile along the x'-axis a correction factor is used and calculated as follows and illustrated in Figure 22 below.

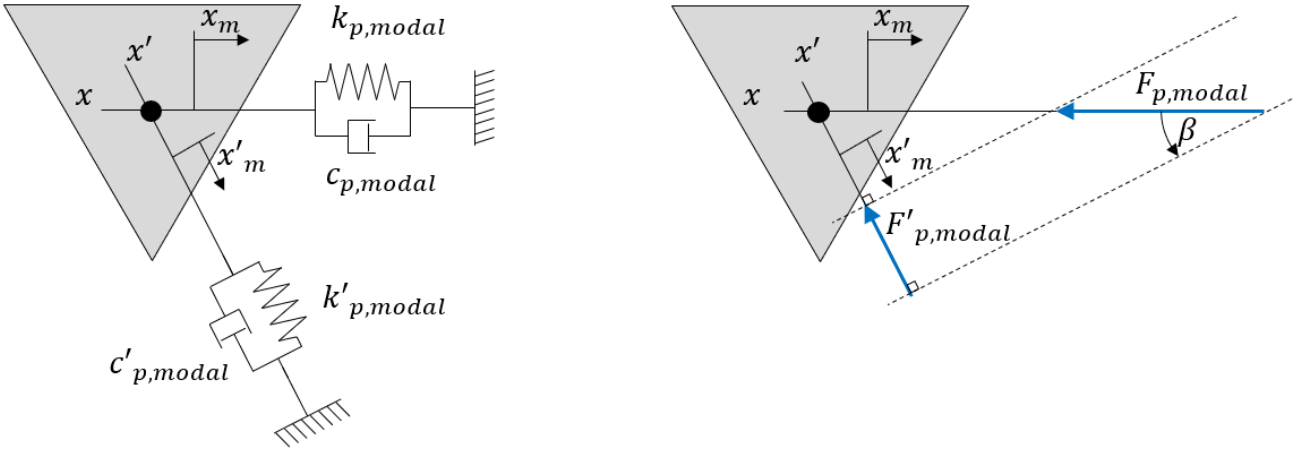

Figure 22: Modal transformation of pile properties to x'-axis

$$F'_{p,modal} = F_{p,modal} \sin\beta$$

$$F_{p,modal} = k_p x_m + c_p \dot{x}_m$$

$$x_m = x'_m \sin\beta$$

$$F_p = k_p x'_m \sin\beta + c_p \dot{x}'_m \sin\beta$$

$$F'_p = \left(k_p x'_m + c_p \dot{x}'_m\right) \sin^2\beta$$

The modal properties of the pile can be incorporated into the one-dimensional model along the x'-axis when corrected with a factor $sin^2\beta$.

6.3. Equations of motion

In Figure 23 below an illustration is given of the one-dimensional model. The mass m is the mass of the tip (m_t) plus the modal mass (m^*) of the pile multiplied with the correction factor:

$$m = m_t + m^* sin^2\beta$$

The spring k_e is the combined spring constant of the soil and pile modal spring stiffness, calculated as follows:

$$k_e = k_{e,soil} + k_{p,modal} sin^2\beta$$

The damper c_e is the combined damping constant of the soil and pile modal damping, calculated as follows:

$$c_e = c_{e,soil} + c_{p,modal} sin^2\beta$$

$x_m$is the horizontal displacement of the oscillating mass, $F_{fr,applied}$ is the applied force on the plastic element, x_f is the resulting plastic displacement, F_{cr} is the yield force of the soil and c_f is the damping constant of the soil in the plastic region. The system has two states, stick where only elastic displacements occur and slip where the soil is plastically deformed. Below the equations of motion for each state are given and the criteria of state transition.

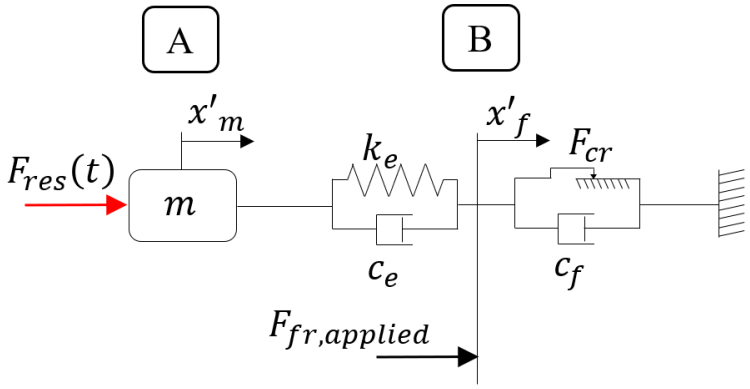

Figure 23: one dimensional model of the pile tip and the soil

State 1 – Stick
When the friction element is not activated, $\dot{x_f}$ is zero. Therefore the equation of motion for stick at A becomes:

$$m\ddot{x_m} + c_e\dot{x}_m + k_e(x_m - x_f) = F_{res}(t)$$

Transition stick to slip
If the force acting on the friction element is larger than the critical force the model enters state 2.

$$F_{fr,applied} > F_{cr}$$

The applied force, $F_{fr,applied}$, to the plastic element is:

$$F_{fr,applied} = k_e(x_m - x_f) + c_e\dot{x}_m$$

State 2 – slip
If the friction element is activated the system has the following equations of motion at A and at B:

A. $m\ddot{x}_m + c_e(\dot{x}_m - \dot{x}_f) + k_e(x_m - x_f) = F(t)$
B. $c_e(\dot{x}_f - \dot{x}_m) + k_e(x_f - x_m) + c_f\dot{x}_f + F_{cr}\left(sgn(\dot{x}_f)\right) = 0$

Transition slip to stick
The transition from state 2 to state 1 occurs when the direction of the motion of slider element attempts to change direction, which coincides with a change in the sign of the velocity.

$$sign\left(\dot{x}_f(t)\right) \neq sign\left(\dot{x}_f(t - dt)\right)$$

6.4. Penetration distance of the pile per cycle

From the vertical component of the plastic soil deformation along the x'- axis the penetration of the pile per cycle is calculated. The penetration per cycle is also effected by horizontal component in combination with the geometry of the pile tip. An schematic of this effect is shown in Figure 24 below. In picture 1 the

oscillation cycle starts and in 2 the plastic soil deformation after one oscillation cycle is visualized with the blue dots on either side.

The soil deformation occurs symmetrically all around the pile. From the model, the value of the soil deformation per cycle along the x'- axis, dx'_f, is calculated. With this value the penetration per cycle, dz, is calculated as follows. The vertical plastic soil deformation distance is calculated with:

$$dz_{x'_f} = dx'_f \cos\beta$$

The soil also deforms in horizontal direction. This displacement causes a vertical penetration, dz_{geo}, related to the geometry of the pile tip and is calculated with:

$$dx'_{f,x} = dx'_f \sin\beta$$
$$dz_{geo} = dx'_{f,x} \frac{1}{\sin\alpha}$$

The total vertical penetration per cycle is the combined penetration due to the horizontal and vertical components of the plastic soil deformation and calculated with:

$$dz = dz_{x'_f} + dz_{geo}$$
$$dz = x'_f \left(\cos\beta + \frac{\sin\beta}{\tan\alpha}\right)$$

Interesting to see that if the pile tip were to be flat, $\alpha = 90^0$ and $1/\tan\alpha$ is zero. In this situation no penetration would take place due to plastic horizontal soil deformation.

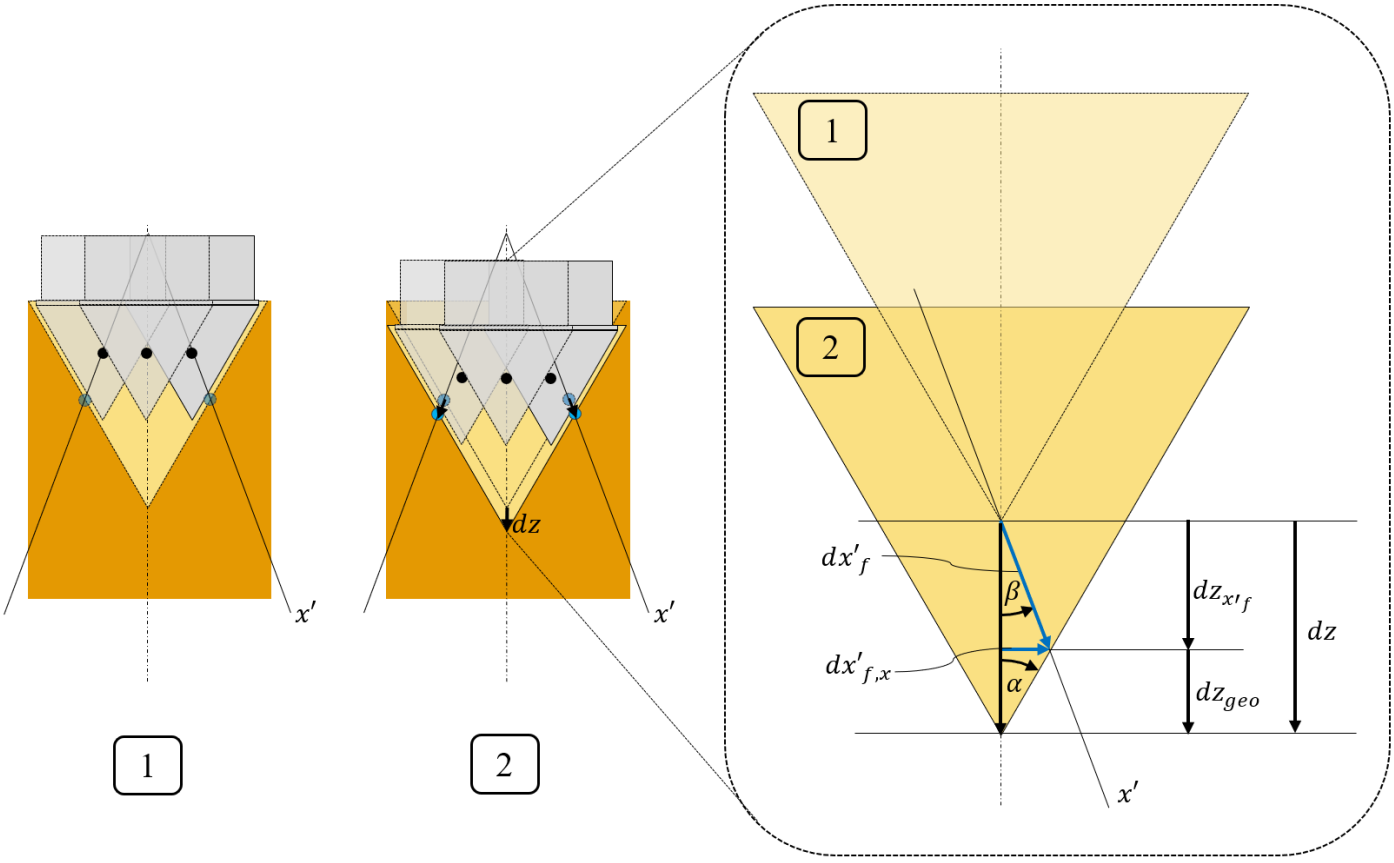

Figure 24: Penetration of the pile into the soil per oscillation cycle of the eccentric mass.

6.5. Description of soil input parameters

The input parameters of model the soil represented in the Kelvin-Voigt element are the spring- and radiation damping constants. In the nonlinear slider-damper element the material damping constant and yield strength are captured. In this section these input parameters are further explained and orders of magnitude for all four input parameters are given.

6.5.1. Spring constant

The spring constant can be derived from the steepness of the hysteresis diagram in the elastic region as described in section 3.2. This steepness is the secant shear-modulus of the soil. At very small strains G = G_{max}, [18]. For larger strains and an increasing number of loading cycles the secant shear modulus decreases. Penetration of the pile into the ground causes large strains in the soil and a high number of loading cycles occur due to the oscillating element. The maximum shear modulus is therefore most likely an overestimation. However, it will be used as a value to start the calibration of the model. Knowing the pile and soil properties the initial backbone curve can be calculated with the P-y curve method[13] which is illustrated in Figure 25.

$$P = C_1 p_u tanh\left(\frac{kH}{Ap_u} y\right)$$

Where

P	is the resistance of the soil per meter
C_1	is the factor to account for cyclic loading conditions
p_u	is the ultimate resistance per meter
H	is the depth
k	is the initial modulus of subgrade reaction
y	is the lateral deflection, or strain

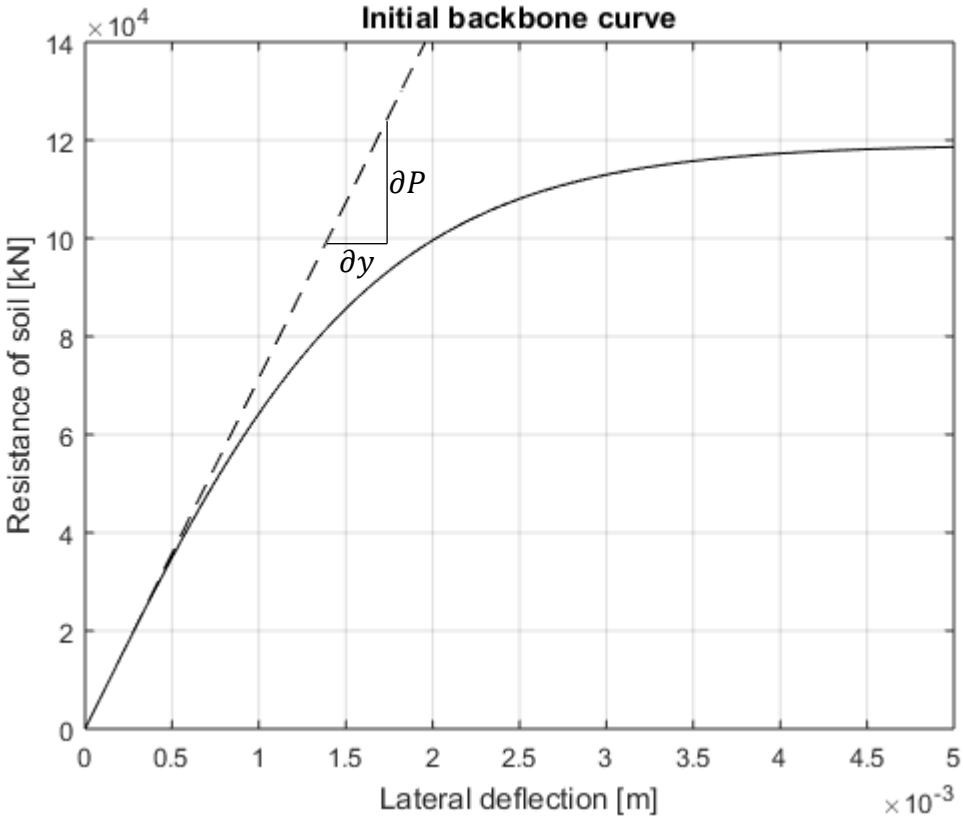

Figure 25: Calculation of the maximum spring constant of the soil at the Maasvlakte site at the maximum depth the prototype could reach.

The dimensions of the prototype and properties of the soil provide a spring constant of an order of magnitude of 10^7.

6.5.2. Radiation damping

The soil damper in the Kelvin-Voigt element represents the dissipation of energy due to radiation damping. The energy of the wave radiating outwards due to small strain visco-elastic soil motion. The value of the damping constant is taken so it will be non-reflective:

$$c_{e,soil} = \rho A V$$

Where ρ is the density of the soil, A is the horizontal surface area of the cone and V is the shear wave velocity in the soil. The shear wave velocity in the soil at the test location can be expressed with the obtained CPT data by a formula developed by [21]:

$$V = 25.3\ {q_c}^{0.163} {f_s}^{0.029} D^{0.155}$$

Where q_c and f_s are the cone resistance and shaft friction in kPA and D is the depth in meters. The formula is empirically established with experiments in Holocene sand with an R^2 of 0.75. At the test site a cone resistance of up to 30 MPa was found with a friction ratio of approximately 0.5%. These values provide a radiation damping constant in the order of 10^3 – 10^4. A description of the soil conditions can be found in Appendix A – Soil at test location.

6.5.3. Material damping

Material damping in soil is associated with plastic deformation of the soil. Mechanisms that contribute to material damping are friction between soil particles, strain rate effect and nonlinear soil behavior. The area between the stress-strain hysteresis loop is defined as the dissipated energy for one cycle of loading. A hysteresis loop is shown in Figure 7. The magnitude of the material damping constant will be iteratively determined with the results of the experiments.

6.5.4. Yield force of soil

The yield force of the soil is defined in the penetration model as the force that needs to be applied to the slider-damper element before plastic deformation sets in. The quantity of the yield force will be determined empirically.

6.6. Simulation

The software used to model the system is MATLAB. The ode45 function in combination with event functions is used to calculate the solution of the system of equations. The event functions model the transition from slip to stick and back.

7. Calibration of the penetration model

The input values for the penetration model that are explained in section 6.5 are calibrated with the results obtained from the experiments. The measured parameters used to calibrate the penetration model are the accelerations in the tip, the rotational speed of the eccentric mass, the force exerted by the winch and the penetration depth over time. From the design of the prototype the structural properties of the prototype are known.

7.1. Methodology

The penetration model requires multiple input parameters of the prototype and the soil. The input parameters of the prototype are split into structural-, operational- and dynamic response properties. Structural- and dynamic response properties are fixed during a certain experiment. Operational properties can vary during experiments. The dynamic response properties of the prototype are represented in the KV-element together with the small strain visco-elastic soil properties. The high amplitude rate dependent soil behavior and resulting pile penetration into the soil is captured in the plastic element.

Due to the large number of input variables, the calibration of the model is performed in stages. For every stage the parameters of the preceding stages are used. Therefore, the stages are ordered by the certainty of the calculation. In theory the dynamic response of the prototype is a fixed property, however, the values are obtained from less accurate measurements.

1. Structural properties of the prototype
2. Operational properties of the prototype
3. Dynamic response properties of the prototype as input for the KV-element
4. Small-strain visco-elastic soil behavior input for the KV-element
5. High amplitude plastic soil behavior leading to the pile penetration

7.2. Stage 1 –Structural properties of the prototype

The structural properties of the prototype are fixed and shown in Table 8 below. Only the eccentric moment will be varied over the experiments but not during an experiment, therefore it is classified as a structural property.

Table 8: Properties of prototype

parameter	symbol	Value	Unit
Mass of tip	m_t	100	kg
Modal mass of pile	m^*	44.3	kg
Modelled mass	$m = m_t + m^* sin^2\beta$		kg
Length of pile	L	5	m
Cross-sectional area of pile	A	0.0047	m^2
Density of steel	ρ	7850	kgm^{-3}
Low eccentric moment	me	0.005	kgm
Medium eccentric moment	me	0.010	kgm
Large eccentric moment	me	0.015	kgm
Angle of cone tip	α	30	degrees
Width of base of cone tip	B	0.275	m

7.3. Stage 2 – Operational properties of prototype

The operational properties of the prototype are the rotational speed and the winch force. These are obtained from the experiments of all three eccentric mass configuration. Plots of the winch force and the rotational speed of all experiments are shown in Figure 26 to Figure 31 below.

The winch is pre-tensioned to keep the winch cable tightly around the guidewheels. This pre-tension of 2 kN is clearly visible in all three figures at zero depth. The force is limited by the torque of the winch motor. During most experiments, the winch motor was operated at full torque. This is visible for the low and medium eccentric mass experiments, after 1.5 meters penetration the full winch force is mobilized by the soil resistance and no significant fluctuation occurs.

The winch force during the large eccentric mass experiments shows a large fluctuation over depth and per experiment. Causes for this are mentioned earlier in Chapter 5. Based on the observations above, an average winch force of all experiments is taken as an input for the penetration model.

The rotational speed of the motor was controlled by a proportional hydraulic pressure valve. During all experiments this proportional valve was set to the maximum of 300 bars. The resulting rotational speed was quite similar for all experiments for a given eccentric mass configuration. Therefore, an average rotational speed is taken per eccentric mass configuration as an input for the penetration model.

A summary of the winch force and rotational speeds per eccentric mass configuration are presented in Table 9 below.

Table 9: Average rotational speeds and winch forces per eccentric moment configuration

parameter	**Eccentric mass**	**symbol**	**Value**	**Unit**
Average rotational speed	Small	$\omega_{avg,low}$	1,200	rad/s
	Medium	$\omega_{avg,med}$	1,100	rad/s
	Large	$\omega_{avg,large}$	840	rad/s
Average winch force	All	F_{winch}	17.0	kN

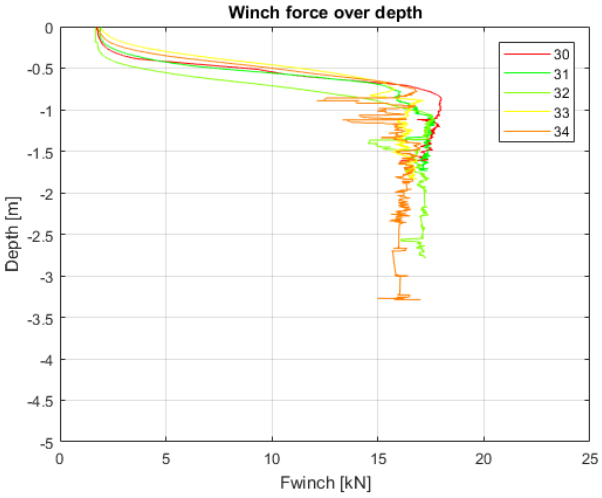

Figure 26: Winch force for small eccentric moment configuration

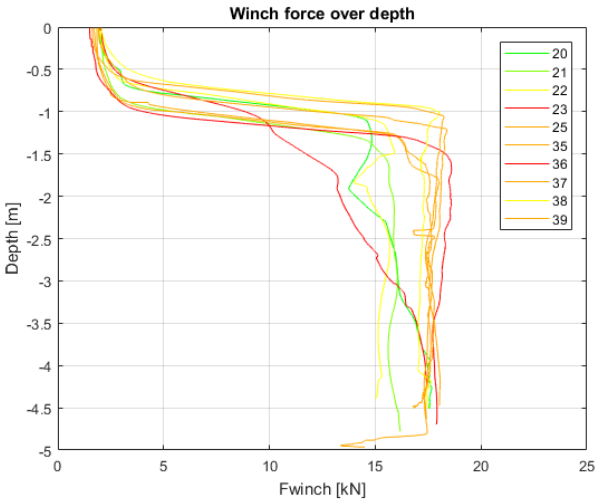

Figure 27: Winch force for medium eccentric moment configuration

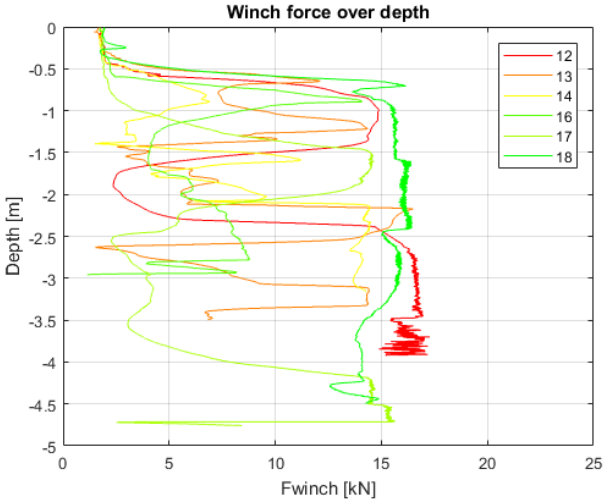

Figure 28: : Winch force for large eccentric moment configuration

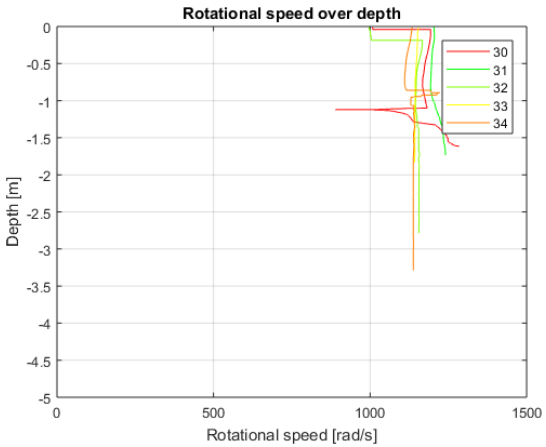

Figure 29: Rotational speed for small eccentric moment configuration

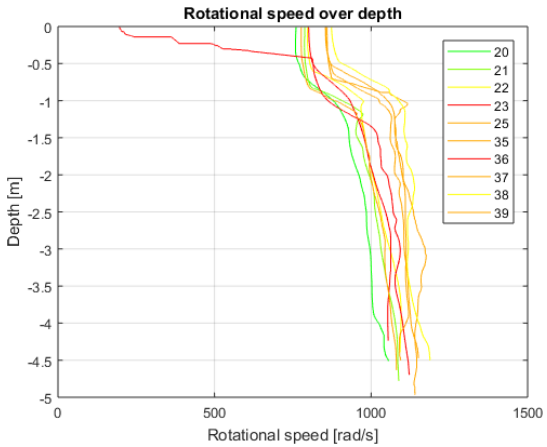

Figure 30: Rotational speed for medium eccentric moment configuration

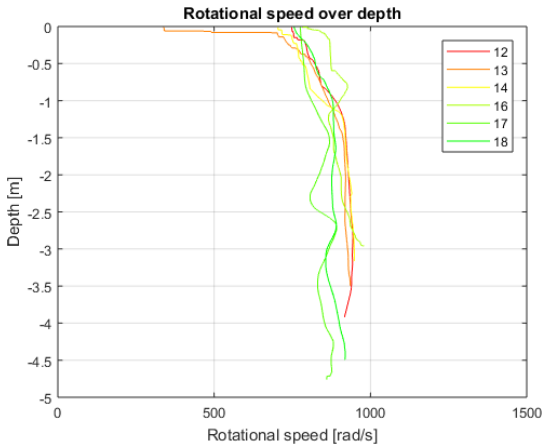

Figure 31: : Rotational speed for large eccentric moment configuration

7.4. Stage 3 – Dynamic response properties of the prototype

The prototype system has a certain dynamic response to the rotating eccentric mass. To quantify the dynamic response and to determine the natural frequencies of the system a frequency response analysis is performed. To isolate the prototype properties an experiment without soil interaction is analyzed.

During one experiment with the low eccentric mass, the rotational speed was varied from zero to maximum while the prototype pile was suspended in the air. In Figure 32 the amplitude-frequency characteristic of the prototype is shown. A large peak between 800 and 900 rad/s is clearly visible, indicating a natural frequency of the prototype system at 865 rad/s. With the natural frequency at 865 rad/s, the mass of the tip (m_t) and the modal mass of the pile (m^*) the spring constant of the prototype system is calculated:

$$k_{p,modal} = (m_t + m^*)\omega_n^2 = (100 + 44.3) \cdot 865^2 \cong 10^8 \, {}^{N}/_{m}$$

Plotting the static amplitude times the dynamic amplification factor over the frequency with the following formula, while iteratively determining the damping ratio to match the peak value at 865 rad/s provides the red line in Figure 32 below.

$$|X| = x_{static}\left(\left(1 - \frac{\omega^2}{\omega_n^2}\right)^2 + \gamma^2 \frac{\omega^2}{\omega_n^2}\right)^{-1/2}$$

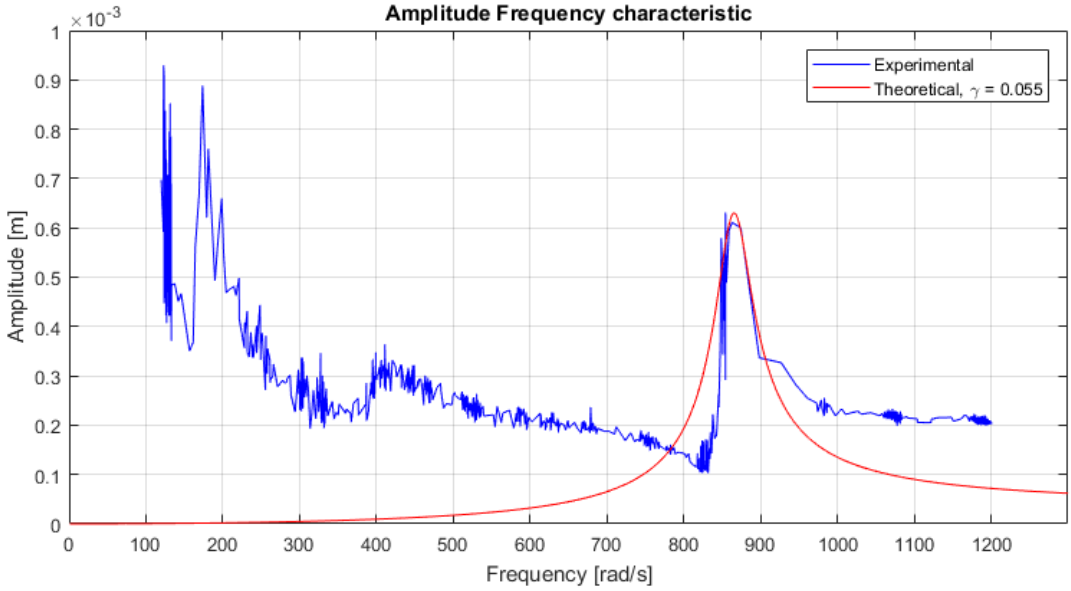

Figure 32: Amplitude of the tip oscillating in the air, plotted against the rotational speed of the small eccentric mass

Where x_{static} is calculated with the magnitude of the eccentric force and the modal spring constant of the pile:

$$x_{static} = \frac{F_{ecc}}{k_{p,modal}} = \frac{me\omega^2}{k_{p,modal}}$$

The damping constant of the pile is calculated with:

$$c_{p,modal} = \frac{1}{2}\gamma\sqrt{k_{p,modal} \cdot m} = 3{,}500 \; {}^{Ns}/_{m}$$

A summary of the dynamic response properties of the prototype are given in Table 10 below.

Unexpected high amplitudes at lower- and higher frequencies are also observed and can be explained with the following:

1. Multiple natural frequencies at lower frequencies, the pile is assumed to be rigidly connected to the top of the piling rig. However, observations showed that significant play existed between the guidance of the pile and the pile rig.
2. Measurement error in the hydraulic oil flow meter with which the rotational speed is calculated; at lower flow rates this sensor was not accurate.

Table 10: Dynamic response properties of prototype

Dynamic response parameter of prototype pile	symbol	Value	Unit
Spring constant	$k_{p,modal}$	10^8	$[N/m]$
Damping ratio	γ_{pile}	0.055	$[-]$
Damping constant	$c_{p,modal}$	3,500	$[Ns/m]$

7.5. Stage 4 – Small strain visco-elastic behavior of the soil

The spring coefficient of the small strain soil-pile interaction is given in section 6.5.1 and is in the order of:

$$k_{e,soil} = O(10^7)\ [N/m]$$

The decrease of the secant shear modulus due to cyclic loading as described in section 3.2 would further decrease the spring constant of the soil, this will be taken into account during the calibration of the model.

The damping constant of the small strain visco-elastic behavior of the soil is defined as the radiation damping and calculated in section 6.5.

$$c_{e,soil} \cong O(10^3 - 10^4)\ \left[{}^{Ns}/_{m}\right]$$

7.6. Stage 5 – High amplitude plastic soil behavior

The calibration of the values of the critical force and the material damping constant during plastic deformation is performed by iteratively finding similar average penetration speeds and similar amplitudes of the oscillations, shown in Table 13 below. By varying two input parameters, two output parameters must be found. A corresponding penetration speed can be found by adjusting the critical yield force and material damping constant in the slider-damper element. However, looking at the amplitude-frequency characteristics in Figure 32 the amplitudes of the oscillations at the average rotational speed of 1200 rad/s are not possible to match with a natural frequency of 865 rad/s. Therefore, the following assumption is made:

The natural frequency found at 865 rad/s is not the only natural frequency of the system. Otherwise the high amplitudes cannot be explained for higher and lower rotational speeds than 865 rad/s. Since the model is one-dimensional, providing only one natural frequency, for all three eccentric mass simulations the excitation frequency and natural frequency are taken as equal. Also the damping- and spring constant of the KV-element are expressed in the natural frequency and the damping ratio to minimize the number of input parameters. With the input values given in Table 11 the calibration was started.

Table 11: penetration model input parameters for calibration of the slider-damper element

Model input parameter	Symbol	Quantity/calculation	Unit
Excitation frequency(i)	ω_{small}	1,200	$[rad/s]$
	ω_{medium}	1,100	$[rad/s]$
	ω_{large}	840	$[rad/s]$
Eccentric moment (i)	me_{small}	0.005	$[kgm]$
	me_{medium}	0.010	$[kgm]$
	me_{large}	0.015	$[kgm]$
Natural frequency	ω_n	$\omega_n = \omega_i$	$[rad/s]$
KV spring constant	k_e	$m{\omega_n}^2$	$[N/m]$
KV damping constant	c_e	$0.5\gamma\sqrt{km}$	$[Ns/m]$

The values presented in Table 12 below, return the best match between the experimental and modelled values.

Table 12: Slider-damper element input parameters of the prototype-soil system

Model input parameter	Symbol	Quantity/calculation	Unit
Damping ratio of KV-element	γ	0.10	$[-]$
Material damping constant	c_f	300,000	$[Ns/m]$
Yield force of soil	F_{cr}	30,000	$[N]$

The modelled penetration diagrams combined with the penetration diagrams from the experiments are shown in Figure 33, Figure 33 and Figure 35 below. Also the modelled oscillations at a smaller time scale are given in Figure 32, Figure 34 and Figure 38 below.

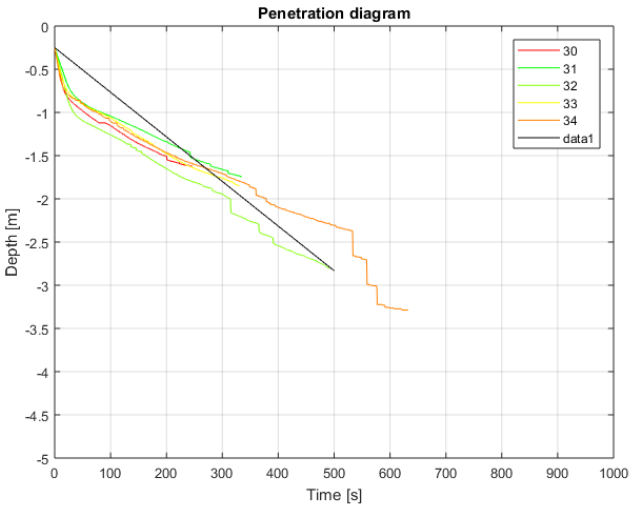

Figure 33: Large time scale modelled penetration with small eccentric moment

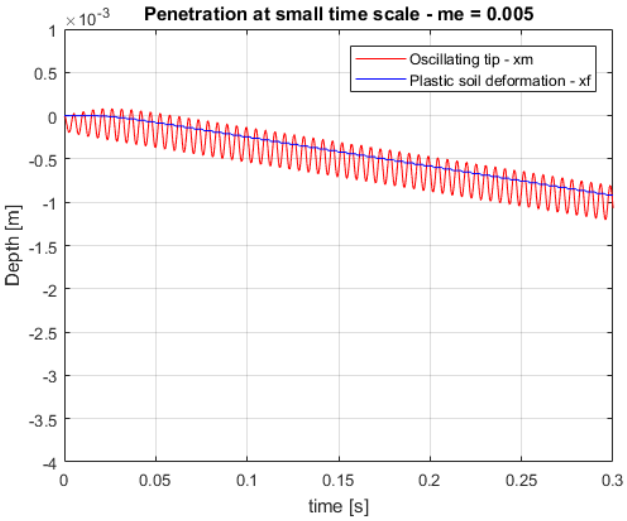

Figure 34: Small time scale modelled penetration with small eccentric moment

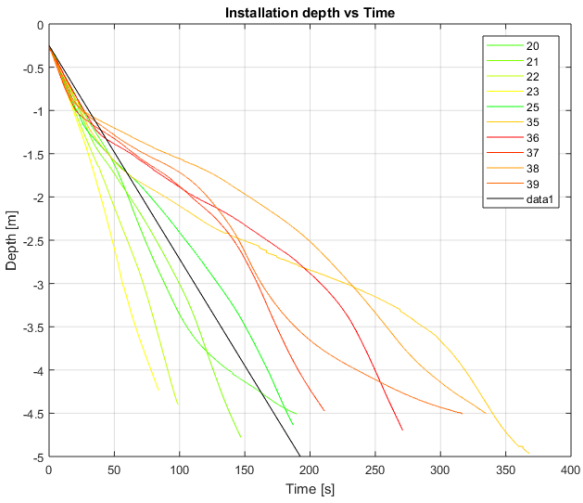

Figure 35: Large time scale modelled penetration with medium eccentric moment

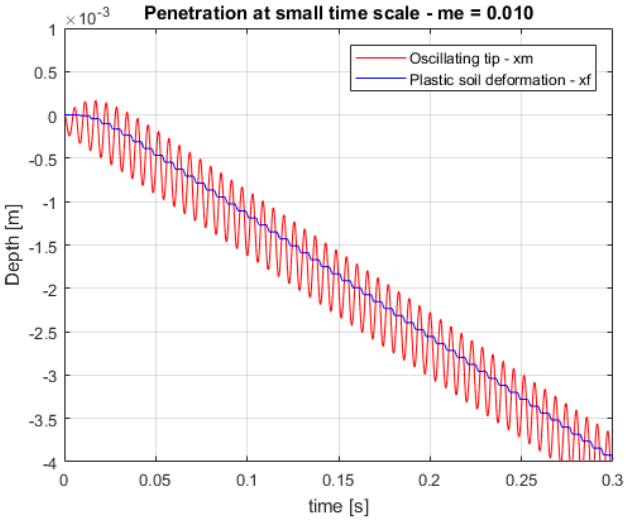

Figure 36: Small time scale modelled penetration with medium eccentric moment

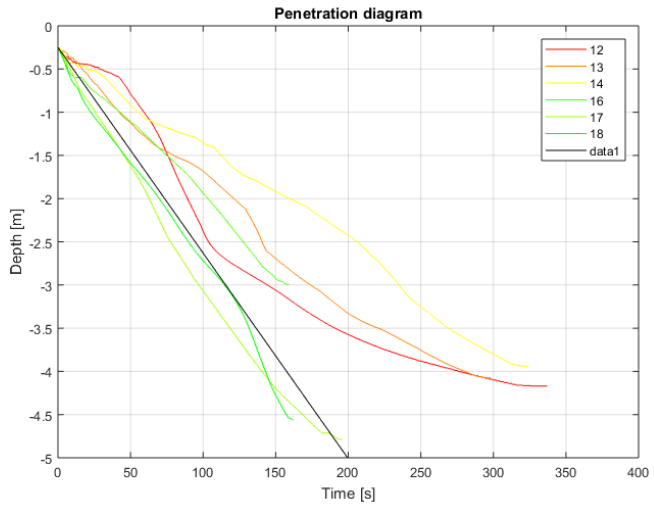

Figure 37: Large time scale modelled penetration with large eccentric moment

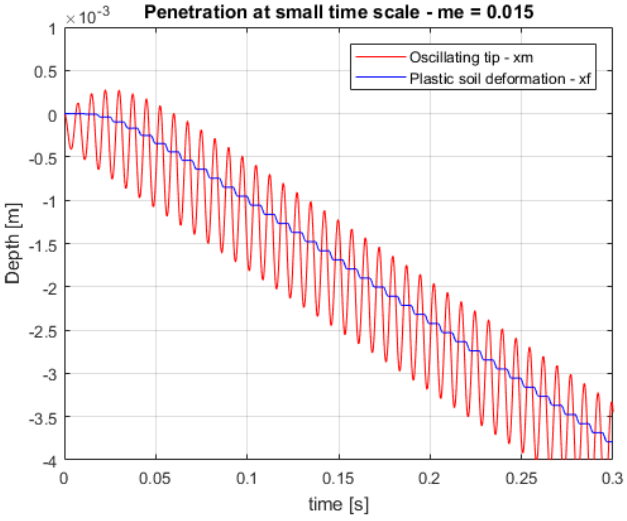

Figure 38: Small time scale modelled penetration with large eccentric moment

7.7. Penetration model validation

To determine whether the proposed penetration model suffices as a model to predict the penetration of the prototype pile and the oscillating motions of the tip, the following criteria are used.

1. Capability of modelling measured oscillations and the correct dependency on fluctuating exciting force
2. Capability of modelling measured penetration speeds and the correct dependency on fluctuating exciting force

In Table 13 below a comparison between the modelled penetration speed and average measured penetration speed is given. Also the modelled and average measured amplitudes of the oscillating tip are given.

Table 13: Average penetration speeds and amplitudes of the three eccentric mass configurations

Eccentric mass configuration	Average penetration speed [mm/s]		Single amplitude [mm]	
	Experiments	Model	Experiments	Model
Small	3.10	5.0	0.20	0.20
Medium	23.0	25.0	0.45	0.35
Large	18.2	23.8	N/A	0.60

7.7.1. Modelling of penetration

Most noticeable in the results of the penetration model is the same drop in penetration speed for the large eccentric weight, compared to the medium eccentric mass. Also the very low penetration speed for the low eccentric mass configuration is produced by the model. Therefore, the penetration model seems to be quite adequate to predict the experiments.

7.7.2. Modelling of oscillations

In Figure 39 and Figure 40 below the amplitude-frequency characteristic of the small and medium eccentric mass respectively is shown. The modelled amplitudes and the measured amplitudes correspond pretty well, also the increase in amplitude for an increase in eccentric mass is correctly modelled. Unfortunately, no useful measurements were produced to calculate the amplitude of the large eccentric mass configuration experiments.

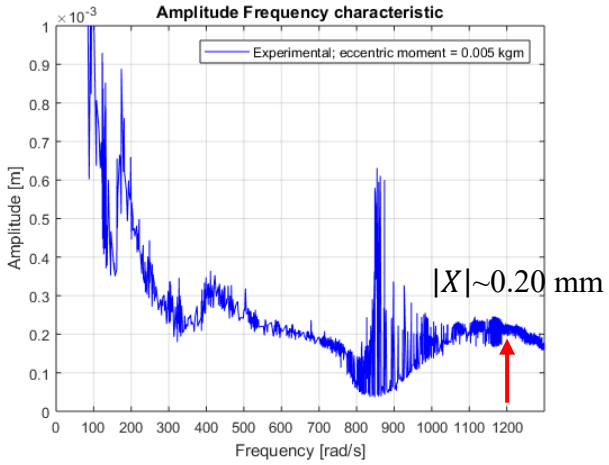

Figure 39: Amplitude-frequency characteristic of penetration with small eccentric mass. Amplitude at 1200 rad/s is approximately 0.2 mm.

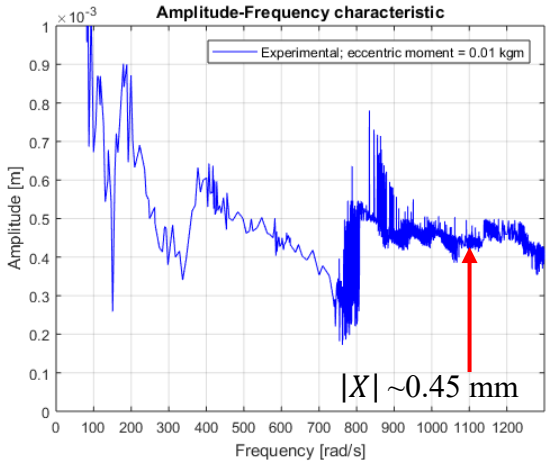

Figure 40: Amplitude-frequency characteristic of penetration with medium eccentric mass. Amplitude at 1200 rad/s is approximately 0.45 mm

The adjustment of the natural frequency to the exciting frequency is a weakness in the model. This could be solved with a 2- or even 3-dimensional model with multiple natural frequencies.

8. Conclusions & Recommendations

The conclusions of this research and recommendations for further research are given in this chapter.

8.1. Conclusion

In the sections below conclusions are drawn on the technical- and commercial feasibility.

8.1.1. Technical feasibility

The experiments have shown that pile penetration to a depth of 4.5 meters is possible with a prototype pile with one segment of the vibro-drill. The reduction of the tip- and shaft resistance with the vibrating element and the lubrication layer is effective enough to penetrate the pile into the soil.

Effectiveness of the reduction of soil resistance

A way to express the effectiveness of the soil resistance is to compare the soil resistance of the prototype to the cone resistance found in the CPT measurements. With a maximum downward force of 20 kN and a frontal surface area of 0.059 m^2 the maximum static pressure of the tip onto the soil was 337 kPa. The average cone resistance at the location was 15 MPa. This is almost a factor 50 higher. Therefore, the reduction in soil resistance to driving with the prototype compared to static penetration of the cone penetration test is considered very effective.

Loading characteristics

The experiments and the model show that the penetration speed is primarily dependent on the magnitude of the eccentric force. This force was highest for the medium weight configuration and returned the highest average penetration speed. The least effective configuration was the small eccentric mass, which generated the lowest eccentric force and was not capable of penetrating to the target depth.

Pile refusal

Two clear reasons for pile refusal can be identified; dense soil with high cone resistance values and experiments without water injection. The water injection will therefore be incorporated in future designs of the Vibro-drill. Very dense soil will be in the area of application. Therefore, a solution must be found for these types of soil.

Optimizations for future Vibro-drill prototypes

From the model and observations during the experiments a number of optimizations are identified for the next prototype of the Vibro-drill. These potential optimizations will be subject to further research.

The amplitude of the oscillations of the pile tip were much higher than expected. From the analysis of the data it appeared that the prototype was operating close or within a natural frequency. The model confirms this, because the results of the experiments can only be approached with the model by setting the excitation frequency to the natural frequency. Implementing this is the design will increase the effectiveness of the Vibro-drill.

The angle of the tip will most likely also influence the performance. From the model a factor is a factor, related to the tip angle, is derived. A small tip angle will displace the soil predominantly horizontally to the side, but will increase the surface area and therefore decreases the magnitude of the applied load. A large angle will displace the soil more downwards, which is less effective but the magnitude of the applied load will increase due to the smaller surface area.

The ratio between the eccentric force and vertical push force also affects the performance in the model. Here an optimum is found were the push force is not too high but also not too low compared to the eccentric force.

Lateral bearing capacity

The lateral bearing capacity is higher than the predicted bearing capacity with the P-y curve method which is an unexpected but positive outcome. The lateral and also, when necessary, the vertical bearing capacity will be subject to further research.

8.1.2. Commercial feasibility

The answers to the questions concerning the commercial feasibility are given below.

Can the vibro-drill decrease the Sound Exposure Level (SEL)?

Measurements taken during the experiments show a noise level of 89 dB, a 21 dB decrease compared to a similar pile installed with a hammer in land. This is a good qualitative indication of the potential noise reduction at sea. However, the comparison is not entirely representative due to the following reasons:

1. Test were conducted on land, noise underwater propagates differently.
2. The vibrating tip is rigidly connected to the pile, causing the entire pile to vibrate and creating more noise. The elements on the vibro-drill will be flexibly connected so the pile itself will only show minimal vibrations.

Can the vibro-drill increase the penetration speed of the foundation pile?

The penetration speed of the prototype is higher than conventional piling. The average penetration speed of the best configuration was 23 mm/s with peaks of up to 50 mm/s. The average penetration speed of a foundation pile with a hydraulic hammer is 5 mm/s. A small remark has to be made here, the penetration is only tested to 4.5 meters depth. With increasing depth the soil resistance to penetration also increases, the penetration speed will therefore decrease. If the high penetration speed is to be maintained during the entire penetration of 35 meters adaptations to the machine must be made.

Can the vibro-drill decrease the handling time?

The Vibro-drill could decrease the handling time. The vibro-drill is already attached to the foundation pile, therefore the handling steps are reduced. The installation, in chronological order, will be the lifting of the pile, placing it into the gripper frame, activating the vibro-drill until target depth is reached and finally detaching the crane hook. The entire lift and retrieval operation of the hammer is eliminated.

Can the vibro-drill decrease the high fluctuating stresses in both number and amplitude?

Yes, calculated in section 5.7 the maximum stresses are calculated. These are well below the fatigue limit of steel. The number of stress cycles does increase, but since the stresses are below the fatigue limit no fatigue is caused.

Can the vibro-drill decrease the mass of the foundation pile due to a simpler design?

Yes, the mass of the foundation pile can be decreased. As mentioned in section 1.1 the fatigue damage is in the range of 10% - 20%. Without fatigue damage, potentially the mass of the pile can be decreased by approximately the same percentage.

The conclusions based on this research indicate that the Vibro-drill is a potential viable alternative to the current installation methods. A summary of the performance of the Vibro-drill prototype is added to the comparison of the performance of current pile driving techniques in Table 14 below.

Table 14: Comparison of the performance of pile driving techniques

Criteria	Impact hammer	Vibratory hammer	Blue Piling hammer	Vibro-drill (potentially)
Sound Exposure level (SEL)	-	+	+	+
Penetration speed	+/-	+	+	+
Handling time	-	+	N/A	+
Fatigue damage	-	+	+	+
Reduction in mass	-	+	+	+
Penetration capability	+	-	N/A	+
Lateral bearing capacity	+	-	N/A	+

8.2. Recommendations

Recommendations for future research are given in this section.

8.2.1. Recommendations for future experiments:

Conduct tests in more types of soil. The soil in at Maasvlakte II was dense sand. In the area of application, the North Sea, also clay layers and rocks are found.

A larger test range is necessary to fully determine the technical feasibility of the Vibro-drill. This test range must be extended to at least 40 meters to capture the monopile installation market.

The test location was situation on land, the area of application is offshore. Test in an underwater environment are therefore required for further development.

Noise measurements must be conducted during test underwater. The majority of the noise will be probably originate from the seismic noise of the vibrating elements below the sea surface.

Conduct more CPT measurements at the nest test site. The large spread in the results of the experiments could be due to very local fluctuations. In this way these can be captured. Boring samples are also addition to further evaluating the performance in certain soil conditions and to more accurately determine the angle of internal friction and the relative density.

A more detailed analysis of the test results will gain further insights into the performance and working principles. For example an per experiment on all factors such as the absorbed power, fluctuations over depth, cone resistance at that exact spot etc.

Incorporate the design optimizations mentioned in the conclusions in the next prototype.

8.2.2. Recommendations for future modelling:

Calibrate the model for every test separately with the corresponding CPT values to find a correlation between the model inputs and CPT measurements.

Incorporate the lubrication layer into the model. The shaft resistance will play an increasingly larger role with an increasing penetration depth range. Also the occurrence of possible preference flows must be researched.

Create a more detailed model with at least a horizontal and vertical dimension. Allocate different soil properties to the horizontal- and vertical soil deformations. With this model the natural frequencies can be more accurately estimated. This model should include the monopile foundation.

The soil weakens due to the cyclic loading. A quantification of the degradation of the soil must be incorporated into the model to more accurately determine the effectiveness of the cyclic loading.

Bibliography

[1] R. A. Kastelein, “Effect pile driving on porpoise hearing,” no. September, pp. 1–17, 2014.
[2] OSPAR, “OSPAR inventory of measures to mitigate the emission and environmental impact of underwater noise Biodiversity Series,” p. 41, 2014.
[3] S. Schrocht, “Technical Noise Mitigation during Offshore-Windfarm Foundation Installation Examples from Offshore Windfarms,” no. October, pp. 1–18, 2015.
[4] A. Tsouvalas, *Offshore noise generated by pile driving*, no. november. 2015.
[5] Pondera Consult, “Underwater noise caused by pile driving. Impacts on marine mammals, regulations and offshore wind developments,” p. 73, 2014.
[6] NOAA, “Underwater Noise,” no. June, 2014.
[7] C. LeBlanc, “Vibro-driving of large diameter offshore piles: a feasible installation concept for the future?,” *Geotech. Eng. Offshore Wind - Danish Geotech. Soc. Semin.*, no. April, 2014.
[8] M. F. Deeks, A.J., Randolph, “Analytical modelling of hammer impact for pile driving,” *Int. J. Numer. Anal. Methods Geomech.*, vol. 17, no. 5, 1993.
[9] A. A. Rodger and G. S. Littlejohn, “A study of vibratory driving in granular soils,” *Géotechnique*, vol. 30, no. 3, pp. 269–293, 1980.
[10] V. Whenham and A. Holeyman, “Load Transfers During Vibratory Driving,” *Geotech. Geol. Eng.*, vol. 30, no. 5, pp. 1119–1135, 2012.
[11] L. de Neef, P. Middendorp, and J. Bakker, “Installation of monopiles by vibrohammers for the Riffgat Project,” *Piling Symp.*, pp. 1–14, 2015.
[12] J. Gattermann, V. Herwig, and C. Moormann, “VIBRO Project - Vergleich des lateralen Tragverhaltens von vibrierten und geschlagenen Stahlrohrpfählen in sandigen Böden,” 2015.
[13] API, “Recommended Practice for Planning , Designing and Constructing Fixed Offshore Platforms — Working Stress Design,” *Api Recomm. Pract.*, vol. 24–WSD, no. December 2000, p. 242, 2007.
[14] A. Holeyman, “Keynote lecture: Vibratory driving analysis.” 2000.
[15] D. J. Dunn, “Fluid Flow Theory,” no. 1, pp. 1–34.
[16] K. Wessel, S. Dam, L. Bo, and K. W. Sørensen, “Behaviour of Cohesionless Soils During Cyclic Loading Amir Shajarati,” 2012.
[17] K. H. Andersen, “Bearing capacity under cyclic loading — offshore, along the coast, and on land.,” *Can. Geotech. J.*, vol. 46, no. 5, pp. 513–535, 2009.
[18] M. Vucetic and R. Dobry, “Effect of Soil Plasticity on Cyclic Response,” *J. Geotech. Eng.*, vol. 117, no. 1, pp. 89–107, 1991.
[19] W. Borst and T. Vellinga, “The Monitoring Programme for the Maasvlakte 2 - Construction at the Port of Rotterdam,” *Terra Aqua*, no. 129, pp. 16–29, 2012.
[20] A. Verruijt, “Grondmechanica,” 1993.
[21] R. D. Andrus, N. P. Mohanan, P. Piratheepan, B. S. Ellis, and T. L. Holzer, “Predicting shear-wave velocity from cone penetration resistance,” *Proc. 4th Int. Conf. Earthq. Geotech. Eng.*, no. 1454, p. 12, 2007.
[22] D. R. Bosch and R. R. Sotelo, “Determination of Stratigraphy — Soil Types — Using Cone Penetration Test in Sedimentary Deposits in North-East of Argentina,” no. August, pp. 134–139, 2015.
[23] M. Jamiolkowski, D. C. F. Lo Presti, and M. Manassero, “Evaluation of Relative Density and Shear Strength of Sands from CPT and DMT,” *Soil Behav. Soft Gr. Constr.*, no. 119, pp. 201–238, 2003.
[24] Y. Wang, S. K. Au, and Z. Cao, “Bayesian approach for probabilistic characterization of sand friction angles,” *Eng. Geol.*, vol. 114, no. 3–4, pp. 354–363, 2010.

Appendix A – Soil at test location

At the location the experiments were performed five cone penetration tests were taken. The results of the these tests are shown in this section. The type of soil and properties of the soil such as relative density and the angle of internal friction are determined by interpreting the cone penetration test results. The maximum soil penetration of the prototype was 4.5 meters. The cone resistance found in the test location in this depth range is between 3 and 31 MPa with a friction ratio of 0.3 to 1%. Based on these measurements and the analysis in this appendix the soil can be classified as dense- to very dense sand.

A.1. Soil type

In Figure 41 below the red square indicates the range in which the measured values are found. Soil types associated with these values are sand to silty sand and sand. This interpretation corresponds to the visual observations at the test location and the data available from construction reports[19].

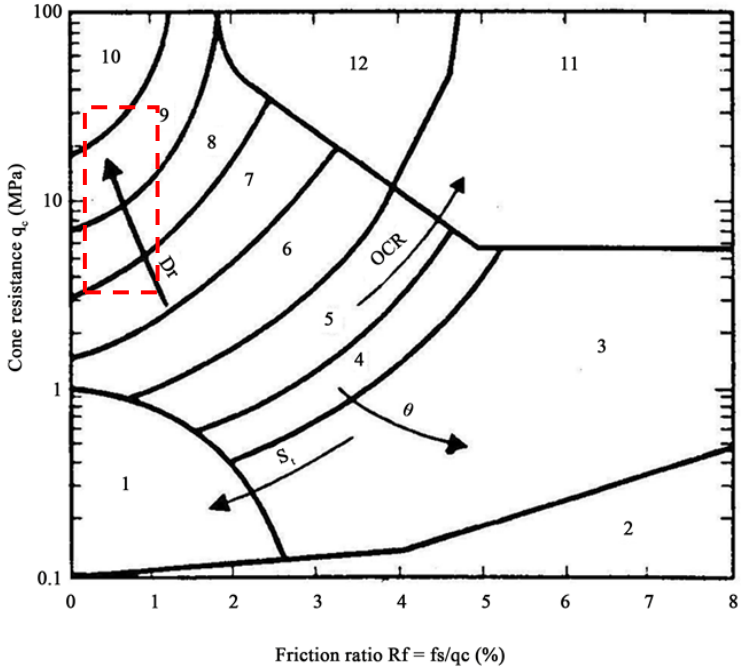

Zone:	Soil Behaviour Type:				
1.	Sensitive fine grained	5.	Clayey silt to silty clay	9.	Sand
2.	Organic material	6.	Sandy silt to clayey silt	10.	Gravelly sand to sand
3.	Clay	7.	Silty sand to sandy silt	11.	Very stiff fine grained*
4.	Silty clay to clay	8.	Sand to silty sand	12.	Sand to clayey sand*

* *Overconsolidated or cemented.*

Figure 41: Soil classification based on CPT data[22]*. Cone penetration test results at the Maasvlakte II fall within the red square.*

A.2. Soil properties

Relevant soil properties for these experiments are the angle internal friction and the relative density. The relative density can be used an indicator for the compressibility of the soil. The angle of internal friction can be used to express the soil strength.

A.2.1. Relative density

The relative density can be approximated with the cone resistance values with the following relation[23]:

$$D_r = \frac{1}{C_2} ln\left(\frac{q_c}{C_0(\sigma')^{c_1}}\right)$$

Where

$C_0 = 181$

C_1 = 0.55
C_2 = 2.61
σ' = effective stress in kPa
q_c = cone penetration resistance in kPa

From this formula a range of relative densities between 40% and 100% are found.

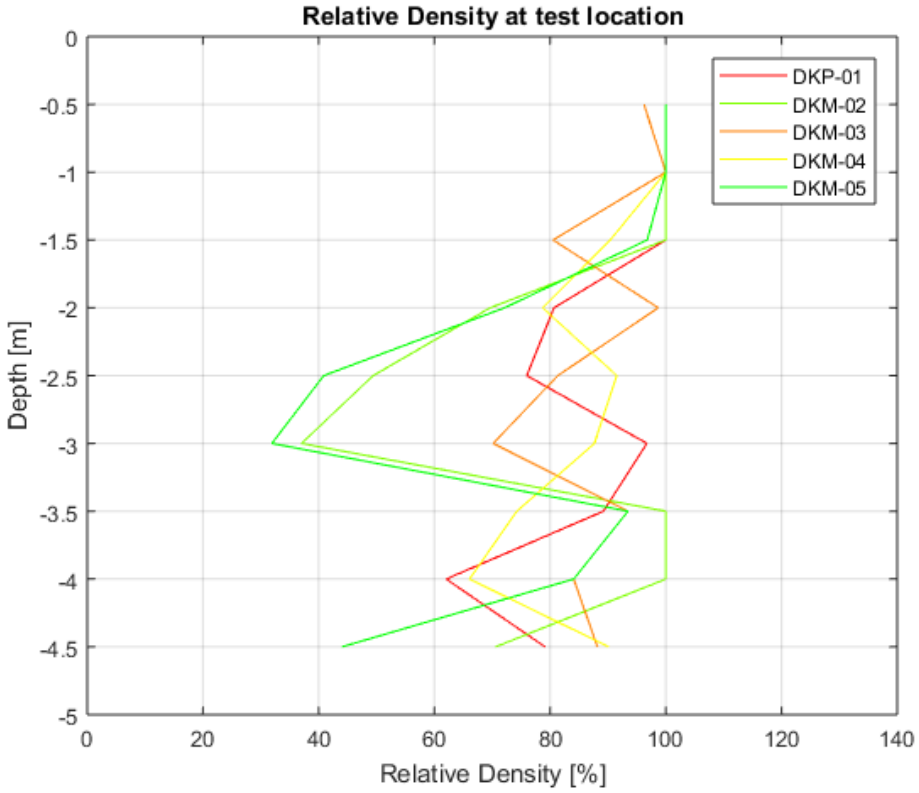

Figure 42: Relative density at test location, determined with the CPT results. Green indicates a low average relative density, red a high relative density

A.2.2. Angle of internal friction

The angle of internal friction at the test location is determined with an empirical relationship between the angle of internal friction, depth and cone resistance[24]. The following formula is used for the relationship.

$$\varphi = 17.6 + 11 \log_{10}\left[\left({}^{q_c}/_{p_a}\right)/\left({}^{\sigma'_{vo}}/_{p_a}\right)^{0.5}\right]$$

Where

p_a is the atmospheric pressure
σ'_{vo} is the effective soil pressure

The angles of internal friction found with this relationship is are between 25 and 45 degrees as shown in Figure 43 below. The average friction angle is around 38 degrees.

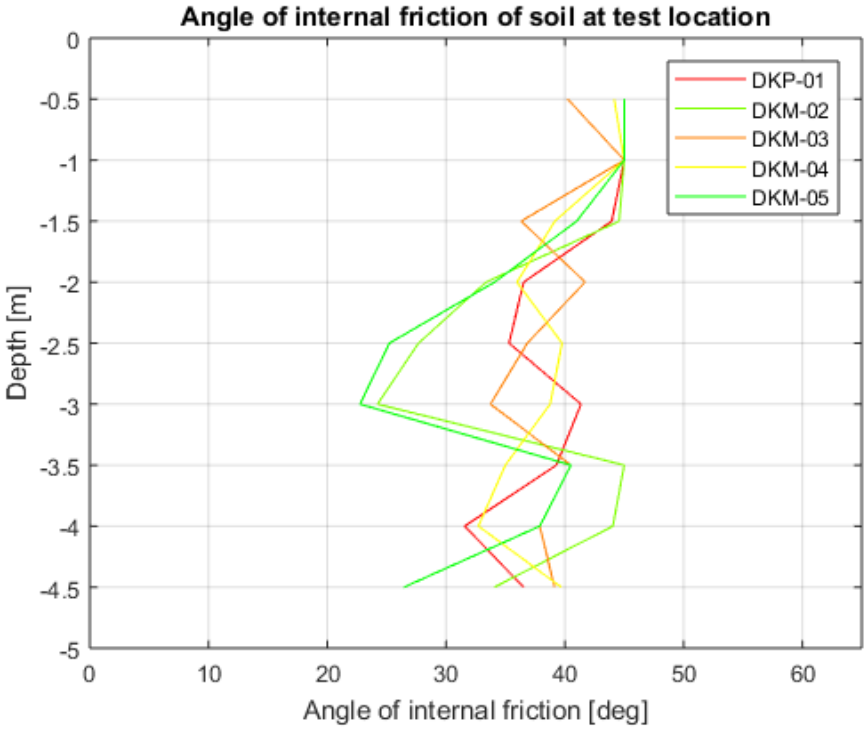

Figure 43: Angle of internal friction derived from the cone penetration tests. Green indicates a relative low average friction angle, red a high relative friction angle.

Appendix B – Prototype design, fabrication and construction

As mentioned in Chapter 4, the length of the pile, the diameter of the tip and pile, the angle of the tip and the amplitude and frequency of the excitation force are the leading considerations in the design of the prototype. Below, the design and the design criteria are further elaborated. Also the fabrication and construction of the prototype is explained.

B.1. Design criteria

The design of the prototype took a multitude of factors into account. These factors are; functionality, reliability, cost, manufacturing, assembly, time and availability of components. The functionality of the prototype comprises the vibrations at the tip and the water lubrication. In Figure 44 below the design flowchart of the prototype is given. The up- and downward guidance in combination with the winch force was incorporated in the piling rig by the manufacturer. The measurement system in further elaborated in Appendix C – Sensors.

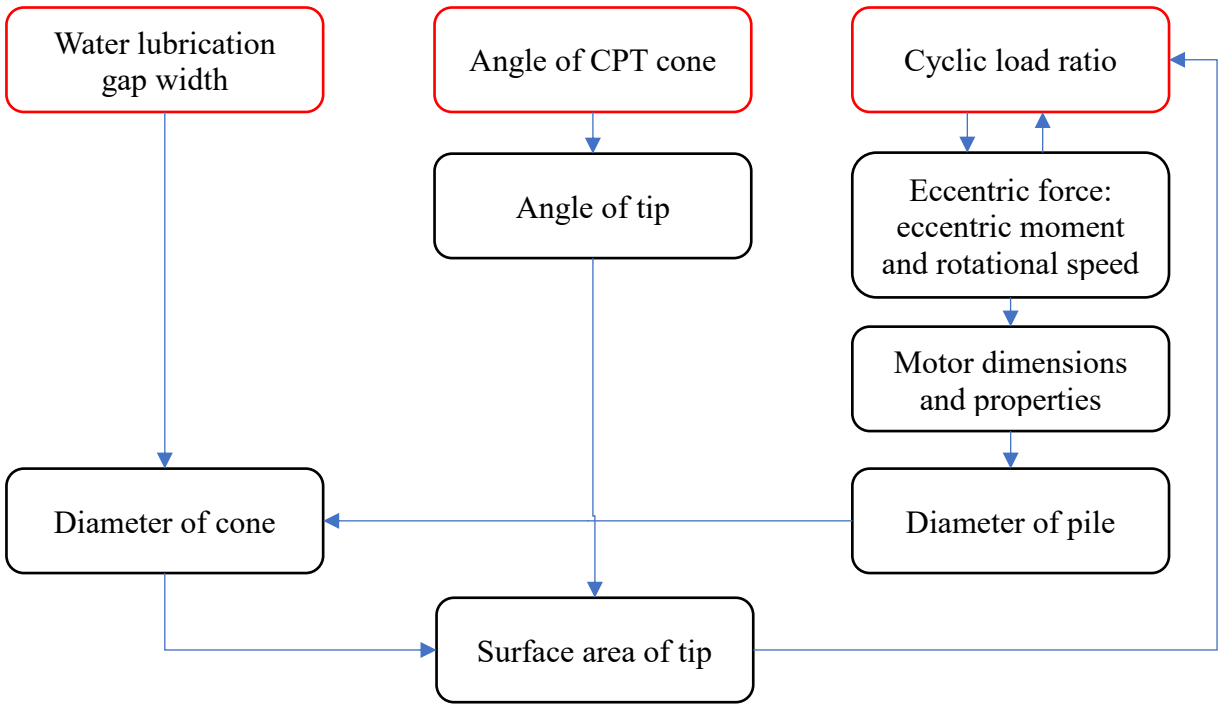

Figure 44: Design flowchart of prototype tip and pile

B.1.1 Water lubrication gap

The water lubrication gap was designed to be 5 mm since the largest soil particles that were expected at the test location are 2 mm. However, due to practical design consideration such as the minimum wall thickness of the pile tip the lubrication gap is wider. The pile diameter is 244.5 mm. The diameter of the tip at its base is 275 mm. An overlap of 10.25 mm is created.

B.1.2 Cyclic load ratio

The eccentric force generated by the rotating eccentric mass creates the oscillating motions of the tip. The magnitude of the eccentric force is a function of the rotational speed and the eccentric moment. To determine the required magnitude of the eccentric force for soil compression and subsequent penetration of the pile, the following calculations and assumptions are made.

The eccentric force acts on the surface area of the tip of the prototype. The surface of the tip is exerting a pressure onto the soil. From Figure 5 the strain contour of sand under cyclic loading is given. For a cyclic loading ratio of 1, which is the applied loading divided by the effective soil pressure, only a few loading cycles are required to generate large strains. Therefore, a minimum loading ratio of 1 is used as a design value. This yield the following design constraint:

$$\frac{Eccentric\ force}{Surface\ area\ of\ tip} > effective\ soil\ pressure = total\ pressure - pore\ water\ pressure$$

This constraint is approached in a conservative manner. The pore water pressure is assumed zero, although water is injected, the tests are performed above sea level in sandy soil. Therefore, it is likely the water will dissipate into the surrounding soil before pore water pressure can be built up.

The maximum effective soil pressure occurs at the maximum penetration depth of 5 meters. The effective pressure at this depth, without pore water pressure, is equal to the total pressure:

$$\sigma = \gamma z = 20\ {}^{kN}/_{m^2} * 5\ m = 100\ kPa$$

If the eccentric force would be static, the applied loading to the soil due to the eccentric force should be at least 100 kPa.

B.1.3 Conical tip dimensions

The main dimensions of conically shaped tip of the prototype are the angle and the diameter of the base. Inside the tip the eccentric weight and several sensors are placed. This is shown in the design overview drawing in Figure 45 below. In this section the considerations for the dimensions of the tip are explained.

Angle

The angle of the tip of the prototype is 60 degrees. This value is chosen as the same angle as the cone of a CPT measurement device. In this manner, a comparison between the two can be more easily made and scaling would only take the change in diameter into account.

Diameter of the tip

The diameter of the tip is chosen a little bigger than the pile diameter to create the gap through which the lubrication water can flow.

Diameter of the pile

The diameter of the pile depends on the size of the hydraulic motor inside the pile. This diameter pile was the smallest possible diameter in which the motor would fit. The smallest possible fit was chosen because a larger diameter would mean more soil displacement. More soil displacement would require more force and again a larger motor.

Length

The length of the pile was chosen as long as possible to enhance the test depth range. However, a longer pile would mean a larger piling rig which is more expensive to rent and more transport cost to Maasvlakte II. A length of 5.4 meters was the maximum length that could fit on the 7.5 meters tall piling rig and was still within financial possibilities.

B.1.4 Up- and downward guidance and winch force

A piling rig was used for the up- and downward guidance of the pile. A winch was attached to the base of the pile frame to pull it up and down. The maximum pull force was set to 17 kN. This force was limited by the own weight of the piling rig, which was 5 mT. More pull force would push one side of the piling from the ground.

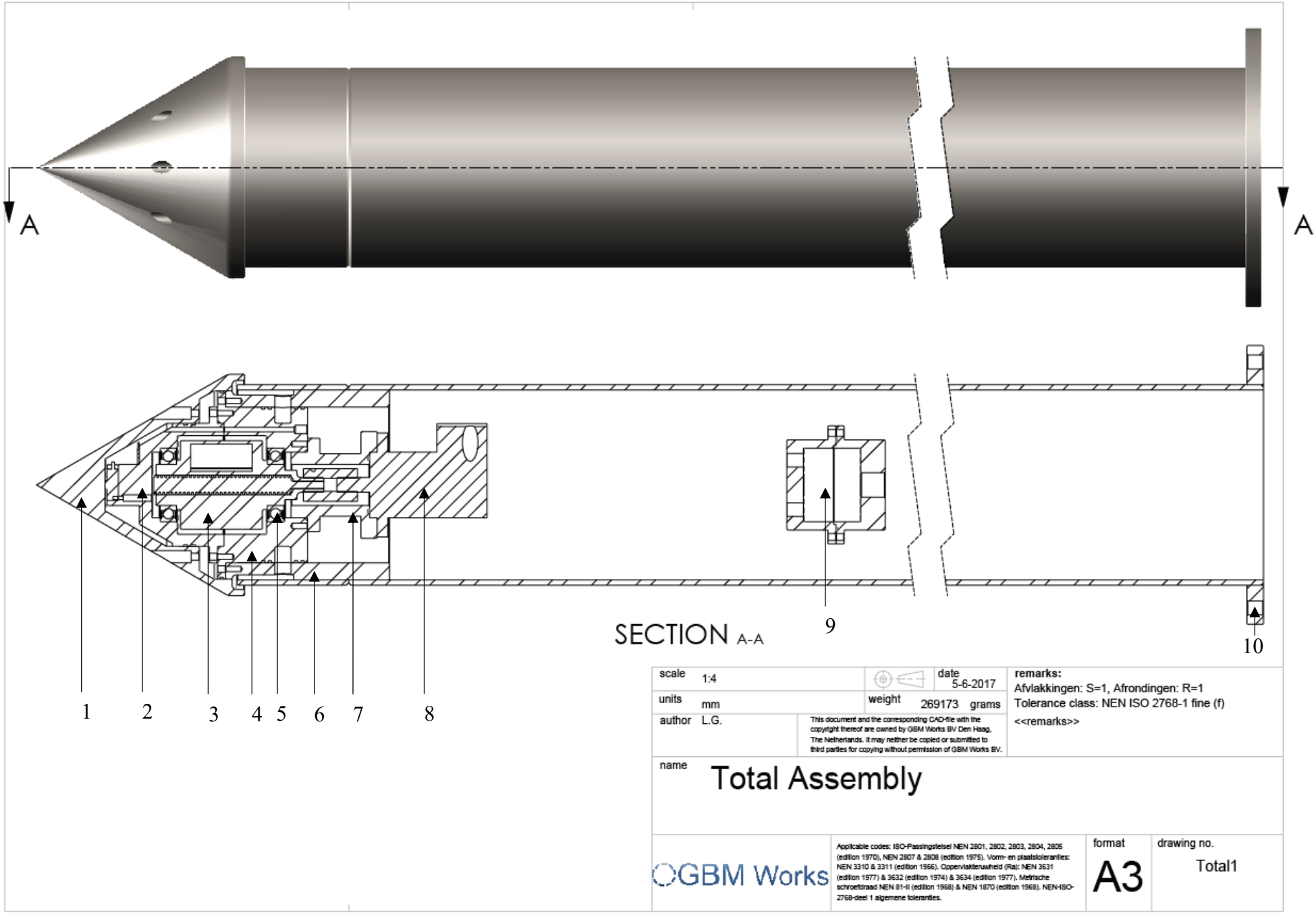

Figure 45: Overview drawing of the prototype design

B.2. Design and fabrication of prototype parts

From the design criteria mentioned in the previous section, the detailed design and engineering of the parts is made. In Figure 45 above the parts are numbered and listed in below. In this section the functions of the parts and design consideration are elaborated. The parts were manufactured by a machine factory and listed in Table 15 below.

Table 15: List of components

#	Part
1	Tip
2	Front housing
3	Eccentric mass
4	Rear housing
5	Bearings for eccentric mass
6	Pile connection bush
7	Bush for the coupling between the motor and eccentric mass
8	Hydraulic motor
9	Water injection splitter
10	Pile connection flange

B.2.1 Tip

The tip is shown in Figure 46 below. The holes are for the bolts to connect the tip to the prototype.

Figure 46: Tip of the prototype pile

B.2.2 Front housing

The front housing of the eccentric mass is shown in Figure 47 below. The button in the middle is a loadcell. This loadcell would measure only the tip resistance. Unfortunately, the loadcell broke down before the first tests were conducted. This was probably due to the high accelerations which it was not designed for.

Figure 47: Front housing of eccentric mass

B.2.3 Eccentric masses

The three eccentric masses are shown in Figure 48 below. They look identical because the part that was cut out is covered with a piece of steel pipe and milled again. The eccentric mass rotated in an oil bath. If the circumference would not be smooth, the resistance of the oil would generate a large power loss.

Figure 48: Eccentric masses for the three configurations; small, medium and large

B.2.4 Rear housing

The rear housing for the eccentric mass is shown in Figure 49 below. In the circumference a large gap is milled to distribute the water over the circumference of the pile before going through the holes in the connection bush, shown in Figure 51 below and eventually upwards along the pile wall. The smaller gaps are for O-rings to keep the water in the larger gap and not into the hollow pile.

Figure 49: Rear housing for eccentric mass

B.2.5 Bearings for eccentric mass

Two bearings are used for the eccentric mass, one is shown mounted in the front housing in Figure 50 below. Simple ball bearings were chosen due to their low cost and robust ball cage design. The experience from the manufacturer was that other ball cages would break due to the vibrations.

Figure 50: Bearing in front housing

Pile connection bush

The bush to connect the prototype to the pile is shown in Figure 51 below. The holes in the circumference allow the water to flow into the soil. The bottom part is welded to the pile.

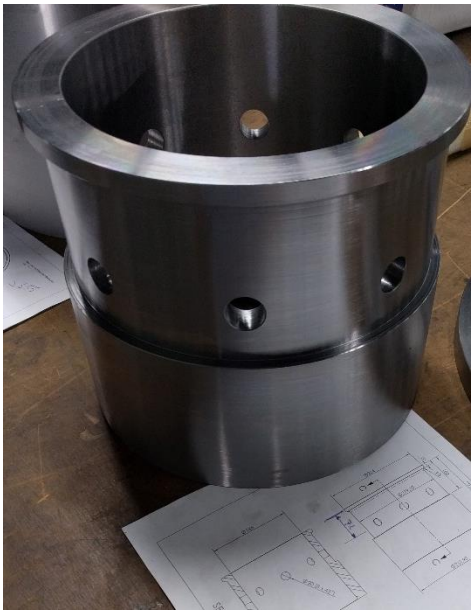

Figure 51: Bush for the connection of the prototype to the pile

B.2.6 Bush for the coupling between the motor and eccentric mass

The bush in which the coupling was positioned between the motor and eccentric mass is shown in Figure 52 below.

Figure 52: Hub for coupling

B.2.7 Hydraulic motor

The hydraulic motor to drive the eccentric mass is shown in Figure 53 below. The motor was chosen for its compact design and high rotation speed range. The maximum continuous rotational speed is 12,800 RPM. At this speed and with a maximum pressure of 300 bars the power output was just over 30 kW.

Figure 53: Hydraulic motor to drive eccentric mass

B.2.8 Water injection splitter

The water was pumped from a tank to the top of the pile and downwards via a single large hose. This large hose is shown in Figure 54 below on the right. The splitter was used to connect 4 smaller hoses and split the water flow. These hoses were connected to the rear housing, were the holes for the connections are visible in Figure 49 above.

Figure 54: Water injection splitter

B.2.9 Pile connection flange

To connect the pile to the pile rig, a flange was welded to the top of the pile, shown in Figure 55 below.

Figure 55: Pile connection flange

B.3. Construction and assembly

The construction of the prototype was done by a piling rig manufacturer that is experienced in building one-off small piling rigs. The assembly of the prototype was done by myself and Nick Noordam, my business partner. Below in Figure 56 an impression of the construction and assembly phase of the prototype is given. At this point the pile was fully assembled and was ready to be mounted onto the piling rig shown in the back.

Figure 56: Impression of the assembly and construction phase of the prototype

Appendix C – Sensors

The sensors that are used to measure the performance of the prototype are elaborated upon in this section. For every sensor the measurement range and accuracy is given. In some cases the sensors were calibrated, a described of this process and the results are given.

C.1. Loadcell

To measure the force of the winch on the pile a S-loadcell was placed between the winch cables with the eye bolts shown in Figure 57 below. The maximum winch force was set at 20 kN. Therefore, a loadcell with a range of 0 to 50 kN was chosen.

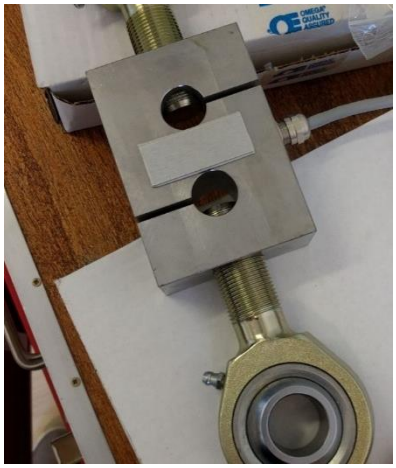

Figure 57: S-loadcell

The loadcell was calibrated with another already calibrated loadcell. This loadcell was placed underneath the pile tip. The winch was operated to its full force while recording both the S-loadcell and the calibrated loadcell. In Figure 58 below the relation is shown. Especially in the lower region the S-loadcell is quite inaccurate. For the higher loads the error is smaller but still considerable.

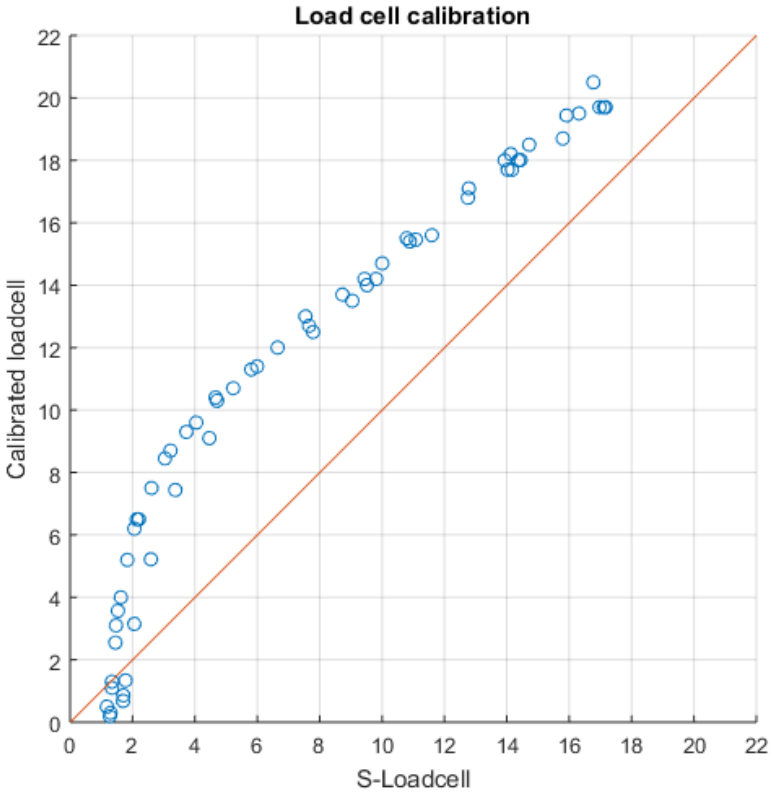

Figure 58: Calibration of S-loadcell

The most likely cause for the error in the loadcell is the manner in which it is attached to the winch cable and guided over the rollers. The cable is guided over two rollers. One of the rollers was positioned at the bottom of the pile rig. The other roller was attached to the guide frame at was quite small. At both rollers the cable was redirected for 180 degrees. This generates extra resistance which is probably the main cause of the error. The extra resistance would cause a reduction in the measured force compared to the calibrated loadcell, which is also observed in the graph.

C.2. Accelerometer

The accelerometer in the tip of the pile was positioned as close to the tip as possible on the front housing of the eccentric mass, shown in Figure 59 below. The measurement range of this accelerometer is ± 200g.

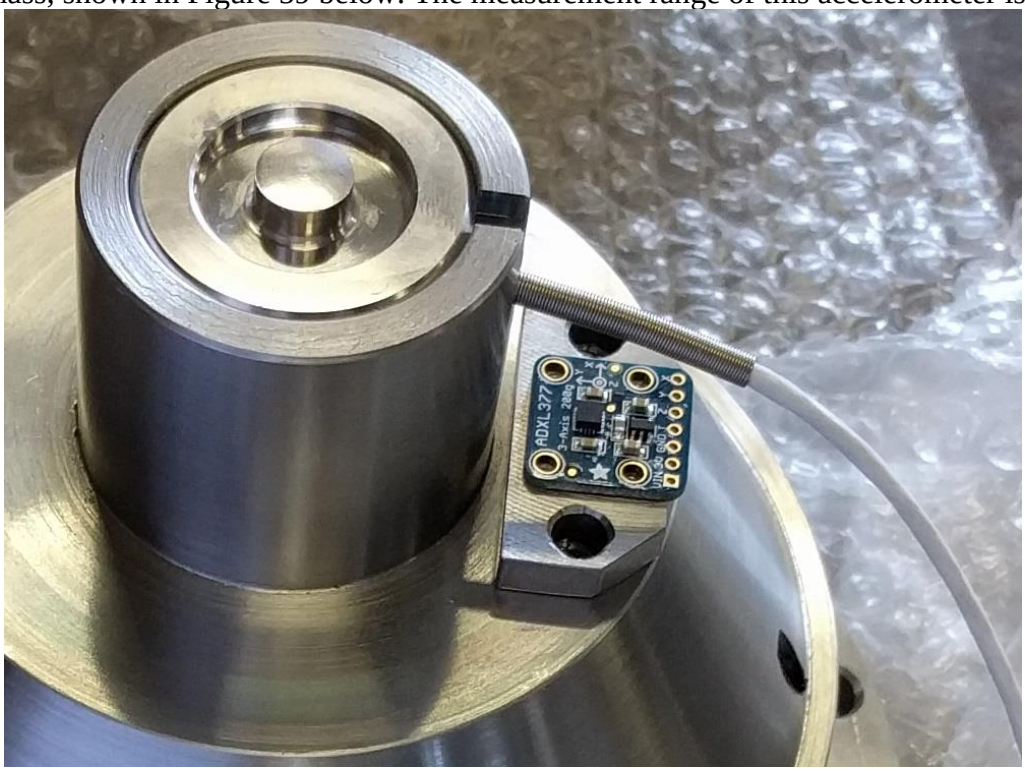

Figure 59: Accelerometer positioned on the front housing in the prototype

C.3. Hydraulic oil flow- and pressure sensor

The hydraulic flow- and pressure sensors are shown in Figure 60 below. The sensors were checked and calibrated with the inhouse developed system of Hydac. The maximum flow to the motor was 70 liter per minute at a pressure of 300 bars. The maximum pressure the sensor could measure was 600 bars, the maximum flow was 600 liters per minute.

Figure 60: Hydraulic flow and pressure sensors

C.4. Depth sensor

To measure the penetration depth of the prototype a pulse wheel was attached to the winch wheel. For every revolution 100 pulses would be sent to the data acquisition unit. The pulse wheel is shown in Figure 61 below. Every revolution of the pulse wheel corresponded to a displacement of 0.5 meters of the pile.

Figure 61: Depth sensor attached to the winch wheel

The pulse wheel was calibrated by moving the pile with the winch over a distance of one meter and counting the number of pulses per meter. The number of pulses per meter were around 200 with a small error margin of one or two pulses.

C.5. Water flow- and pressure sensor

The water flow- and pressure sensor was attached to the main water hose. The sensor was not connected to the main data acquisition unit because the required accuracy was low. Only a general impression of the amount of water used during a test was needed. An analog pressure gauge indicated the pressure. The cumulative flow counter was used to calculate the average flowrate in a test.

Figure 62: Water pressure and flow sensor

Appendix D – Location of experiments and soil conditions

The experiments where conducted with a distance of 3 meters between each other. The locations are shown in Table 16 below. The experiments are numbered in chronological order. Yellow colored squares are experiments without data, incomplete data or corrupted data. The green squares are experiments with usable data. The red squares indicate the locations of the cone penetration tests. The results of the CPT's are presented in Appendix A – Soil at test location.

Table 16: Location of the individual experiments.

	0	3	6	9	12	15	18	21	24	27	30	33	36
0	DKM-03								49		DKM-04		
3				11	12	13	14	15	48	47	46	44	
6			6	7	8	9	17	16	23	22	21	20	
9		1	5	10				18	19	43	26	25	24
12		2	36	37	38	39	30	29	28	27			
15		3				DKP-01	35	34	33	32	31		
18		4	42										
21			41							45			
24			40										
27													
30	DKM-02										DKM-05		

D.1. Summary of CPT data

The results of the experiments are presented with an indication of the soil stiffness at the experiment location. Red for the most stiff location and green for the least stiff location. In this appendix this rating is explained. In Table 17 below the five CPT's taken at the test location are given a stiffness rating. With this stiffness rating the location of every experiment is scored.

Table 17: Summary of CPT data in the test depth range

CPT	Lowest cone resistance [MPa]	Highest Cone resistance [MPa]	Average cone resistance [MPa]	Stiffness rating
DKM-05	3	21	11.1	1
DKM-04	6	23	13.9	2
DKM-01	8	24	14.1	3
DKM-03	8	23	14.4	4
DKM-02	4	31	15.4	5

D.2. Soil conditions at the experiment locations

The soil conditions at the locations of the experiments are scored with a relative stiffness rating. The CPT triangle in which the experiment was conducted and the distance to every CPT location is used as a weighing factor to rate the stiffness at the specific location. In Table 18, Table 19 and Table 20 below the result of this exercise is given. The relative order per configuration is used for the green to red color presentation.

Table 18: Stiffness rating for the small eccentric mass experiments

Experiment	In CPT triangle						Stiffness rating	Order
	Name	Weight	Name	Weight	Name	Weight		
30	DKP-01	0.8	DKM-04	0.2	-	-	2.8	5
31	DKM-04	0.5	DKM-05	0.5	-	-	1.5	1
32	DKP-01	0.4	DKM-04	0.3	DKM-05	0.3	2.1	2
33	DKP-01	0.5	DKM-04	0.25	DKM-05	0.25	2.25	3
34	DKP-01	0.6	DKM-04	0.2	DKM-05	0.2	2.4	4

Table 19: Stiffness rating for the medium eccentric mass experiments

Experiment	In CPT triangle						Stiffness rating	Order
	Name	Weight	Name	Weight	Name	Weight		
20	DKM-04	0.8	DKM-05	0.2	-	-	1.8	2
21	DKM-04	0.8	DKM-05	0.2	-	-	1.8	3
22	DKP-01	0.3	DKM-04	0.6	DKM-05	0.1	2.2	4
23	DKP-01	0.4	DKM-04	0.6	-	-	2.4	5
25	DKM-04	0.7	DKM-05	0.3	-	-	1.7	1
35	DKP-01	0.8	DKM-04	0.1	DKM-05	0.1	2.7	6
36	DKP-01	0.55	DKM-02	0.1	DKM-03	0.35	3.55	10
37	DKP-01	0.7	DKM-02	0.05	DKM-03	0.25	3.35	9
38	DKP-01	0.8	DKM-03	0.2	-	-	3.2	7
39	DKP-01	0.8	DKM-03	0.1	DKM-04	0.1	3.3	8

Table 20: Stiffness rating for the large eccentric mass experiments

Experiment	In CPT triangle:						Stiffness rating	Order
	Name	Weight	Name	Weight	Name	Weight		
12	DKP-01	0.35	DKM-03	0.35	DKM-04	0.3	3.05	6
13	DKP-01	0.4	DKM-03	0.3	DKM-04	0.3	3	5
14	DKP-01	0.35	DKM-03	0.3	DKM-04	0.35	2.95	4
16	DKP-01	0.45	DKM-03	0.1	DKM-04	0.45	2.65	2
17	DKP-01	0.5	DKM-03	0.1	DKM-04	0.4	2.7	3
18	DKP-01	0.6	DKM-04	0.4	-	-	2.6	1